

REPORT DOCUMENTATION PAGE			Form Approved OMB NO. 0704-0188		
<p>The public reporting burden for this collection of information is estimated to average 1 hour per response, including the time for reviewing instructions, searching existing data sources, gathering and maintaining the data needed, and completing and reviewing the collection of information. Send comments regarding this burden estimate or any other aspect of this collection of information, including suggestions for reducing this burden, to Washington Headquarters Services, Directorate for Information Operations and Reports, 1215 Jefferson Davis Highway, Suite 1204, Arlington VA, 22202-4302. Respondents should be aware that notwithstanding any other provision of law, no person shall be subject to any penalty for failing to comply with a collection of information if it does not display a currently valid OMB control number.</p> <p>PLEASE DO NOT RETURN YOUR FORM TO THE ABOVE ADDRESS.</p>					
1. REPORT DATE (DD-MM-YYYY) 06-10-2010		2. REPORT TYPE MS Thesis		3. DATES COVERED (From - To) 6-Oct-2010 -	
4. TITLE AND SUBTITLE Turbulence measurements in the atmospheric surface layer by means of an ultrasonic anemometer and thermometer			5a. CONTRACT NUMBER W911NF-05-1-0398		
			5b. GRANT NUMBER		
			5c. PROGRAM ELEMENT NUMBER 611102		
6. AUTHORS Mario Behn			5d. PROJECT NUMBER		
			5e. TASK NUMBER		
			5f. WORK UNIT NUMBER		
7. PERFORMING ORGANIZATION NAMES AND ADDRESSES University of Massachusetts - Amherst Office of Grant & Contract Admin. 408 Goodell Building Amherst, MA 01003 -3285			8. PERFORMING ORGANIZATION REPORT NUMBER		
9. SPONSORING/MONITORING AGENCY NAME(S) AND ADDRESS(ES) U.S. Army Research Office P.O. Box 12211 Research Triangle Park, NC 27709-2211			10. SPONSOR/MONITOR'S ACRONYM(S) ARO		
			11. SPONSOR/MONITOR'S REPORT NUMBER(S) 49393-EV.11		
12. DISTRIBUTION AVAILABILITY STATEMENT Approved for Public Release; Distribution Unlimited					
13. SUPPLEMENTARY NOTES The views, opinions and/or findings contained in this report are those of the author(s) and should not be construed as an official Department of the Army position, policy or decision, unless so designated by other documentation.					
14. ABSTRACT Mean values and fluctuations of the temperature and the three-dimensional wind vector in the atmospheric surface layer was measured with ultrasonic anemometer/thermometers ("sonics"). The system performance was quantified by comparing observed turbulence spectra with inertial-range spectra predicted by the classical theory of homogeneous and isotropic turbulence.					
15. SUBJECT TERMS ultrasonic anemometer/thermometer, atmospheric surface layer, datalogger, turbulence					
16. SECURITY CLASSIFICATION OF:		17. LIMITATION OF ABSTRACT		15. NUMBER OF PAGES	19a. NAME OF RESPONSIBLE PERSON
a. REPORT UU	b. ABSTRACT UU	c. THIS PAGE UU	UU		Andreas Muschinski
					19b. TELEPHONE NUMBER 413-577-0898

Report Title

Turbulence measurements in the atmospheric surface layer by means of an ultrasonic anemometer and thermometer

ABSTRACT

Mean values and fluctuations of the temperature and the three-dimensional wind vector in the atmospheric surface layer was measured with ultrasonic anemometer/thermometers ("sonics"). The system performance was quantified by comparing observed turbulence spectra with inertial-range spectra predicted by the classical theory of homogeneous and isotropic turbulence.

**TURBULENCE MEASUREMENTS IN THE
ATMOSPHERIC SURFACE LAYER
BY MEANS OF AN ULTRASONIC ANEMOMETER AND
THERMOMETER**

A Thesis Presented

by

MARIO BEHN

Submitted to the Graduate School of the
University of Massachusetts Amherst in partial fulfillment
of the requirements for the degree of

MASTER OF SCIENCE IN ELECTRICAL AND COMPUTER ENGINEERING

February 2006

Electrical and Computer Engineering

**TURBULENCE MEASUREMENTS IN THE
ATMOSPHERIC SURFACE LAYER
BY MEANS OF AN ULTRASONIC ANEMOMETER AND
THERMOMETER**

A Thesis Presented

by

MARIO BEHN

Approved as to style and content by:

Andreas Muschinski, Chair

Neal Anderson, Member

Stephen de Bruyn Kops, Member

Seshu B. Desu, Department Chair
Electrical and Computer Engineering

诗篇， 116:5-7;12-14

耶和华有恩惠，有公义，我们的神以怜悯为怀。
耶和华保护愚人：我落到卑微的地步，他救了我。
我的心哪，你要仍归安乐，因为耶和华用厚恩待你。

我拿什么报答耶和华向我所赐的一切厚恩？
我要举起救恩的杯，称扬耶和华的名。
我要在他众民面前向耶和华还我的愿。

Psalm 116:5-7;12-14

The LORD is gracious and righteous; our God is full of compassion.
The LORD protects the simplehearted; when I was in great need, he saved me.
Be at rest once more, O my soul, for the LORD has been good to you.

How can I repay the LORD for all his goodness to me?
I will lift up the cup of salvation and call on the name of the LORD.
I will fulfill my vows to the LORD in the presence of all his people.

Psalm 116:5-7;12-14

Der HERR ist gnädig und gerecht, und unser Gott ist barmherzig.
Der HERR behütet die Unmündigen; wenn ich schwach bin, so hilft er mir.
Sei nun wieder zufrieden, meine Seele; denn der HERR tut dir Gutes.

Wie soll ich dem HERRN vergelten all seine Wohltat, die er an mir tut?
Ich will den Kelch des Heils nehmen und des HERRN Namen anrufen.
Ich will meine Gelübde dem HERRN erfüllen vor all seinem Volk.

ACKNOWLEDGMENTS

First, I would like to thank my advisor Professor Andreas Muschinski for the guidance, encouragement and the true interest he showed in my work. He had many times made me curious about this for me so new research field and inspired me to learn more about it.

Furthermore, I would like to thank Professor Neal Anderson and Professor Stephen de Bruyn Kops for serving on my thesis committee, for proof reading my thesis and their suggestions.

I would also like to thank Professor Steve Frasier for originally giving me the opportunity to join the Microwave Remote Sensing Lab (MIRSL) and Gordon Farquharson and Fransisco Lopez-Dekker who encouraged me to apply for the Master of Science program. Without them I wouldn't have joined MIRSL.

For proof reading my thesis and providing suggestions, I would like to thank Dragana Perkovic, Yonghun Cheon, Kery Hardwick and Kapil Edke. I would like to extend my thanks to Yonghun Cheon and Kapil Edge for helping me during the experiment setup and the data collection.

Most of all I want to thank my wife Yuru, for her love and encouragement. She enabled me to overcome all challenges I was facing during this time. I couldn't have done this without her.

Mario Behn

University of Massachusetts Amherst, February 2006

TABLE OF CONTENTS

	Page
ACKNOWLEDGMENTS	iv
LIST OF TABLES	vii
LIST OF FIGURES	viii
 CHAPTER	
1. INTRODUCTION	1
1.1 Motivation	1
1.2 History and Current State	2
1.3 Summary of Chapters	3
2. SURFACE LAYER TURBULENCE THEORY	5
2.1 The Structure of Atmospheric Turbulence	5
2.2 Theory of Locally Homogeneous and Isotropic Turbulence	7
2.2.1 Autocovariance Function and Structure Function	7
2.2.2 Power Spectrum	10
2.2.3 Wavenumber Spectrum	11
2.2.4 Integral Scales and Spectral Widths	11
2.2.5 Inertial Subrange and Structure Parameter	12
2.2.6 Locally Isotropic Velocity Fields	14
2.3 Monin-Obukhov Theory	15
2.3.1 Atmospheric Boundary and Surface Layer	16
2.3.2 Roughness length	16
2.3.3 Turbulence Fluxes	16
2.3.4 Turbulence Scaling Parameters	18
2.3.5 Stability Conditions	19
2.3.6 Logarithmic Law of the Wall	19
2.3.7 Profile Correction Functions	20

3. SYSTEM DESCRIPTION	23
3.1 Sonic Anemometer and Thermometer Measurement Principle	23
3.2 Data Logging System	26
3.3 Time Stamp Validation	29
3.4 File Format	34
4. EXPERIMENT SETUP AND DATA ANALYSIS	36
4.1 Experiment Location and Setup	36
4.2 Weather Conditions	36
4.3 Coordinate Systems	38
4.4 Data Preparation	39
4.4.1 Raw Data	39
4.4.2 Averaging Interval	39
4.4.3 Data Rotation	41
4.4.4 Data Detrending	45
4.4.5 Example for Raw, Rotated and Detrended Time Series	46
4.5 Data Analysis	46
4.5.1 Noise Estimation	48
4.5.2 Measurement Errors	54
4.5.3 Autocovariance Function and Structure Function	57
4.5.4 Periodogram and Power spectrum	61
4.5.5 Inertial Subrange and Structure Parameter	68
4.5.6 Integral Time and Length Scales	72
4.5.7 Isotropy	82
5. SUMMARY AND CONCLUSIONS	86
5.1 Summary	86
5.2 Conclusions	87
5.3 Recommendation and Future Work	89

LIST OF TABLES

Table	Page
3.1 Time stamp format	35
3.2 Data format	35
3.3 Debug information	35
4.1 Wind vector components in Reynolds notation	39
4.2 Number of independent samples and accuracy for integral time scale $\tau_i = 5s$	41
4.3 Performance on wind speed from R.M. Young Company (1999)	56
4.4 Performance on temperature from R.M. Young Company (1999)	56
4.5 Atmospheric processes in the micro scale after Orlanski (1975)	57
4.6 Variance computed from time series, direct FFT and ACF FFT	62
4.7 Variance of noise computed from power spectrum and ACF	66
4.8 Standard deviation of noise computed from power spectrum and ACF	66
4.9 C_α^2 computed from power spectra and structure function	71
4.10 Integral scales	75

LIST OF FIGURES

Figure	Page
2.1 Spectrum of atmospheric turbulence; from Garratt (1992) [p.17]	6
2.2 Structure of atmospheric boundary layer; from Garratt (1992)[p.2]	17
2.3 Wind profile in stable, neutral and unstable air; from Kaimal and Finnigan (1994) [p.12]	22
3.1 Sonic anemometer measurement paths and sample volume (Picture: R.M. Young Company (1999))	24
3.2 Ultrasonic transducer and measurement path from Kaimal and Finnigan (1994) [p.247]	24
3.3 Program structure of data logging program	27
3.4 Raw and corrected time stamps from sonic 1 and 2 data and time difference over a time of 4s.	30
3.5 Relative error between both sonics for linear, corrected and raw timestamps.	32
3.6 Drift of PC clock over 66 h.	33
4.1 Experiment setup at Tilson farm facility (Picture: Yonghun Cheon)	37
4.2 Close up of sonics (Picture: Yonghun Cheon)	37
4.3 Sonic coordinate system (Picture: R.M. Young Company (1999))	38
4.4 Three angle rotation method; diagram from Wilczak et al. (2001)	42
4.5 Wind vector components for a 35 min time series block (left column - raw), (center column - rotated), (right column - detrended)	47

4.6	ACF of u, v, w and θ for maximum time lag $\tau = 0.32s$	51
4.7	Time series of detrended temperature θ	52
4.8	Time series of rotated and detrended wind velocity components u, v and w	53
4.9	ACF of u with a maximum time lag $\tau = 600s$ for sonic 1 and 2	58
4.10	Scales of atmospheric processes; after Orlanski (1975); diagram from Foken (2003)[p.5]	59
4.11	Structure function of u with a maximum time lag $\tau = 600s$ for sonic 1 and 2	60
4.12	Real and imaginary parts of periodogram and power spectrum of u time series computed from ACF	63
4.13	Periodogram and power spectrum of u time series computed from ACF	64
4.14	Periodogram and power spectrum of u time series computed directly from time series	65
4.15	Power spectrum of velocity component time series computed directly and from ACF	67
4.16	Power spectrum of temperature time series computed directly and from ACF	68
4.17	Structure parameter of velocity components from structure functions	69
4.18	Structure parameter of temperature $C_\theta^2(\tau)$ from structure function	70
4.19	Structure parameter of velocity components from power spectrum	72
4.20	Structure parameter of temperature from power spectrum	73
4.21	Autocovariance function $B_u(\tau)$ and integral time scale τ_{iu}	76
4.22	Autocovariance function $B_v(\tau)$ and integral time scale τ_{iv}	77
4.23	Autocovariance function $B_w(\tau)$ and integral time scale τ_{iw}	78
4.24	Autocovariance function $B_\theta(\tau)$ and integral time scale $\tau_{i\theta}$	79

4.25	Integral time scale τ_{iu} and mean wind speed \bar{U}	80
4.26	Integral length scale r_{iu}	81
4.27	Ratios between structure functions	83
4.28	Ratios between power spectra	84

CHAPTER 1

INTRODUCTION

1.1 Motivation

The study of atmospheric turbulence is essential for the understanding of many environmental processes, such as transport of heat, momentum and matter. It has major impact on weather and climate modeling and needs to be taken into account for the design and operation of a wide variety of man-made structures, including buildings, bridges, cars and aircrafts. Hence the measurement of turbulence is of high importance.

Wyngaard (1981) describes advantages and disadvantages of several in-situ measurement devices. The described measurement devices include cup-, propeller- and ultrasonic anemometer (sonic). In Muschinski and Lenschow (2001), the sonic anemometer was highlighted as a highly reliable device, which has had significant impact on the research of atmospheric turbulence. However, it has to be installed carefully to avoid resonances that may corrupt the measurement as pointed out by Siebert and Muschinski (2001).

Two sonics described by R.M. Young Company (1999) were purchased, installed on tripods and used to measure atmospheric turbulence data in the surface layer. These sonics will be part of an integrated measurement system. This integrated system will allow the user to take advantage of the capabilities of diverse turbulent measurement systems and provide extended opportunities to study atmospheric turbulence.

1.2 History and Current State

Early work on turbulence was done by Taylor (1938) and Simmons et al. (1938). Kolmogorov (1941a) and Kolmogorov (1941b) describe the energy dissipation of turbulence and the local structure of turbulence, respectively. At the same time, Obukhov (1941) discussed the spectral energy distribution of a turbulent flow.

Later the classical description of surface layer turbulence was published by Monin and Obukhov (1954), providing a generalization of the law of the wall. Monin (1970) gives a review on the research of the ABL, including a summary of what is now known as the Monin-Obukhov similarity theory. An experimental investigation of the profile-functions resulting from the Monin-Obukhov theory and a generalization of the turbulence spectra was given by Kaimal et al. (1972) based on the so called Kansas 1968 experiment.

The theory wave propagation through locally homogeneous and isotropic turbulence was first described by Tatarskii (1961) and Tatarskii (1971). This was an especially important contribution for the later development and understanding of atmospheric and oceanic remote sensing.

Recently, the state of atmospheric turbulence research has been reviewed by Muschinski and Lenschow (2001). They confirmed the major progress made in the 1970s in the field, but also pointed out that since then the growth of the *fundamental* research has significantly slowed down. During the workshop that was the basis of their paper, they identified five areas, that needed further research. One of these was *In-Situ Measurements*. The potential of this area was illustrated by the example of the ultrasonic-anemometer (sonic) and its impact on the research. Another area was remote sensing, illustrated by the impact of *Radar and Lidar Remote Sensing*.

In this context, it should be noted, that while remote sensing techniques can probe a large volume or area of the atmosphere, they often suffer from a coarse resolution compared to in-situ techniques. This is because they measure spatial averages (path averages, area averages, or volume averages) rather than point values. However, to calibrate remote sensors

and to confirm their proper operation, in-situ measurements can serve as a highly accurate reference. Thus the combination of both techniques is mutually beneficial.

In addition, the emerging computer, network, timing and data acquisition technology has opened up a multitude of fundamental research opportunities on turbulence by allowing to better merge data and measurement systems.

1.3 Summary of Chapters

This chapter was an outline of atmospheric turbulence and its importance. It also gave a summary of the historical milestones and the current state of turbulence research.

Chapter two explains the physical structure of turbulence based on the cascading process in section 2.1. The following section 2.2 reviews the classical theory of locally homogeneous and isotropic turbulence. This includes an explanation of the autocovariance function (ACF), the structure function, the power spectrum and the wavenumber spectrum. The integral time and the length scales are discussed as well, as the expected $5/3$ and the $2/3$ laws in the inertial subrange for the power spectrum and the structure function, respectively. Description of the $4/3$ ratio between longitudinal and the transverse components of isotropic turbulence concludes this section. Section 2.3 discusses the Monin-Obukhov theory and gives definitions for the atmospheric boundary layer and the atmospheric surface layer. The impact of the roughness length is discussed. As a next step, the turbulent fluxes and the turbulent scaling parameter are defined. Section 2.3 ends with an explanation of the density stratification and its impact on stability conditions, the logarithmic law of the wall and its generalization with the correction function for different stability conditions.

The third chapter contains a description of the measurement and data storage system. This includes the measurement principle of the sonic in section 3.1, providing a basic understanding of how it extracts temperature and velocity from the environment. Then the data logging software is described by means of a program structure diagram in section 3.2. Fi-

nally the time stamps are validated in section 3.3 and the file format of the storage data is shown in section 3.4, respectively.

In the fourth chapter, the experiment location and the setup are described in section 4.1. A note on the weather conditions during the experiment is included in section 4.2 and the coordinate systems are defined in section 4.3. Section 4.4 explains how the data was prepared for the analysis. The data preparation includes a description of the raw data, a discussion on the averaging interval, the concept of data rotation between coordinate systems and data detrending. Finally an example is given for raw, rotated and detrended data.

In section 4.5 the data is analyzed by determining the noise floor and discussing the measurement accuracy. Followed by a discussion of the autocovariance function and the structure function in time domain representation, the periodogram and the power spectrum are used for a spectral analysis. Based on the time and spectral domain description, the inertial subranges are shown and the velocity and temperature structure parameters are estimated. Finally the length scale and the time scale of turbulence are computed and isotropy is discussed.

The last chapter, five, briefly summarizes the results with view on the theoretical predictions, concludes the validity of the sonic measurements and gives a few suggestions for further improvement for future turbulence measurements with the the presented system.

CHAPTER 2

SURFACE LAYER TURBULENCE THEORY

In this chapter, the basic theory for the analysis of turbulence measurements in the atmospheric surface layer is summarized. In section 2.1 a qualitative description of the structure of turbulence is stated, to provide an understanding for the two components of the surface-layer turbulence theory. These are the *classical theory of locally homogeneous and isotropic turbulence*, reviewed in section 2.2, and the *Monin-Obukhov theory*, discussed in section 2.3.

2.1 The Structure of Atmospheric Turbulence

One simple way to explain the physical process of atmospheric turbulence is to study its spectrum. Figure 2.1 shows schematically a typical turbulence spectrum. The spatial wavenumber κ is a (reciprocal) measure of the size l of the turbulent eddies,

$$\kappa \sim \frac{1}{l}, \quad (2.1)$$

and the wavenumber spectrum is the energy density depending on eddy size. Through Taylor's Frozen Turbulence Hypothesis (Taylor, 1938), which assumes that the mean wind speed \bar{U} is significantly larger than the rotation velocity of the eddies, the equation relating spatial wavenumber κ and frequency ω can be written as

$$\kappa = \frac{\omega}{\bar{U}}. \quad (2.2)$$

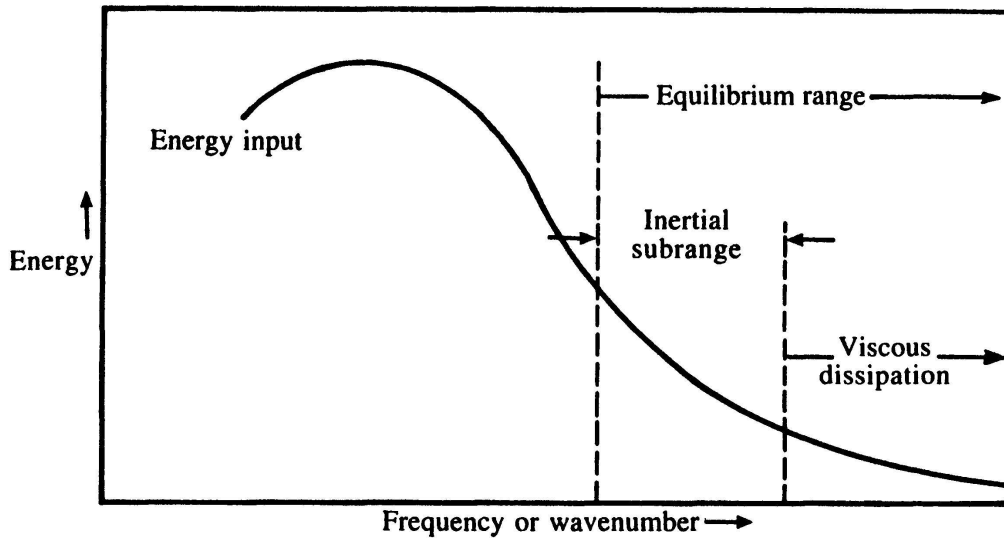


Figure 2.1. Spectrum of atmospheric turbulence; from Garratt (1992) [p.17]

In figure 2.1 three different ranges are shown, the energy input range, the inertial subrange and the viscous dissipation range.

In the energy input range turbulence is created through surface stress resulting in overturning air or through heating or cooling that create convection. In this range the wavenumber or frequency is low, which means that the eddies are large. In the atmospheric surface layer, the boundary of the energy input range to the inertial subrange is typically on the order of meters to tens of meters. Eddies in the energy input range break up and enter the inertial subrange, where they get smaller and smaller through a cascading process. During this process, the kinetic energy is transferred down to smaller scales, but not dissipated. This goes on until the third region, the viscous dissipation range, is reached. Here the eddies get so small that they are converted to heat. The boundary between the viscous dissipation range to the inertial subrange is typically on the order of mm's. In the atmospheric surface layer, the lower and upper boundaries of the inertial subrange are usually estimated as

$$\frac{1}{z} \ll \kappa \ll \frac{1}{\eta_k}, \quad (2.3)$$

where z is the height above ground level(AGL) and

$$\eta_k = \left(\frac{\nu^3}{\epsilon} \right)^{\frac{1}{4}} \quad (2.4)$$

is known as the Kolmogorov scale, where ν is the kinematic viscosity of air and ϵ is the dissipation rate of turbulent kinetic energy per mass unit, or simply the energy dissipation rate.

2.2 Theory of Locally Homogeneous and Isotropic Turbulence

Subsection 2.2.1 introduces the autocovariance functions (ACF) $B_f(\tau)$ and $B_f(r)$, the structure functions $D_f(\tau)$ and $D_f(r)$ for random time functions $f(t)$ and one-dimensional spatial fields $f(x)$, respectively. Here τ is the time lag and r is the spatial lag in the x -direction. In Subsection 2.2.2, the frequency spectrum $W_f(\omega)$ is expressed in terms of $B_f(\tau)$ and $D_f(\tau)$, respectively, by means of the Wiener-Khintchine relationships. Correspondingly, the one-dimensional wave-number spectrum $V_f(\kappa)$ is expressed in terms of $B_f(r)$ and $D_f(r)$ in subsection 2.2.3. The integral time scale τ_i , the integral length scale r_i and the spectral widths of the power spectrum ω_i and the wavenumber spectrum κ_i are defined in subsection 2.2.4. Subsection 2.2.5 introduces the inertial-range laws for $D_f(r)$ and, by means of Taylor's hypothesis, for $D_f(\tau)$. Subsection 2.2.6 gives the inertial-range relationships between the structure functions and the power spectra of the stream-wise velocity u , the lateral velocity v , and the vertical velocity w in the case of locally homogeneous and isotropic inertial-range turbulence.

2.2.1 Autocovariance Function and Structure Function

Following Tatarskii (1971)[p.5], the temporal ACF $B_f(t_1, t_2)$ of a random time function $f(t)$ is defined as

$$B_f(t_1, t_2) = \langle [f(t_1) - \langle f(t_1) \rangle][f(t_2) - \langle f(t_2) \rangle]^* \rangle \quad (2.5)$$

where $\langle \rangle$ denotes the ensemble average and $[\]^*$ denotes the conjugate complex of the quantity in the brackets. t_1 and t_2 are two consecutive measurement times. If $f(t)$ is real and stationary, then $B_f(t_1, t_2)$ can be rewritten as a function of the time lag τ only:

$$B_f(\tau) = \langle [f(t + \tau) - \langle f \rangle][f(t) - \langle f \rangle] \rangle, \quad (2.6)$$

where

$$\langle f \rangle = \langle f(t_1) \rangle = \langle f(t_2) \rangle \quad (2.7)$$

with

$$B_f(\tau) = B_f(-\tau) \quad (2.8)$$

and

$$B_f(\tau) \leq B_f(0) = \sigma_f^2(t) \quad (2.9)$$

where σ_f^2 is the variance (ACF at zero lag). That is, $B_f(\tau)$ is an even function and attains maximum value at $\tau = 0$.

Stationarity means that the statistics of the random process are time-invariant. This implies that variance and mean of the process are assumed to be independent of time:

$$\sigma_f^2(t) = B_f(0) = \text{const.} \quad (2.10)$$

and

$$\langle f(t) \rangle = \langle f \rangle = \text{const.} \quad (2.11)$$

This, however, is not generally the case for surface layer turbulence, because all statistics typically undergo a diurnal cycle. But if the observed time interval is short enough com-

pared to the diurnal cycle, the random process describing the surface layer turbulence can be approximated to have a stationary first increment :

$$F_f(t) = \xi_f(t + T) - \xi_f(t) \quad (2.12)$$

with

$$\xi_f(t) = f(t) - \langle f(t) \rangle, \quad (2.13)$$

which implies that the ensemble average is assumed to vary only linearly with time. From here, there are two possible ways to proceed. The first is to detrend the data, which makes the data stationary again, and to consider the ACF of the detrended process. The second approach is to introduce the structure function $D(t_1, t_2)$ as first suggested by Kolmogorov (1941a):

$$D_f(t_1, t_2) = \langle \{ [f(t_1) - \langle f(t_1) \rangle] - [f(t_2) - \langle f(t_2) \rangle] \}^2 \rangle \quad (2.14)$$

For a linearly varying mean (as assumed with stationary increments) the structure function becomes a function of the time lag $\tau = t_1 - t_2$ only:

$$D_f(t_1, t_2) = D_f(t_1 - t_2) = D_f(\tau) = \langle \{ [f(t + \tau) - \langle f(t + \tau) \rangle] - [f(t) - \langle f(t) \rangle] \}^2 \rangle. \quad (2.15)$$

For the more restrictive case of a constant mean

$$\langle f(t_1) \rangle = \langle f(t_2) \rangle = \text{const.} \quad (2.16)$$

we have

$$D_f(\tau) = \langle \{ [f(t + \tau) - f(t)] \}^2 \rangle. \quad (2.17)$$

For an even more restrictive condition of stationarity, a relation between the ACF and the structure function can be written as:

$$D_f(\tau) = 2[B_f(0) - B_f(\tau)]. \quad (2.18)$$

Similarly, the spatial ACF $B_f(r)$ and the spatial structure function $B_f(r)$ can be expressed:

$$B_f(r) = \langle [f(x+r) - \langle f \rangle][f(x) - \langle f \rangle] \rangle \quad (2.19)$$

and

$$D_f(r) = 2[B_f(0) - B_f(r)], \quad (2.20)$$

where r is the spatial lag in the x -direction.

2.2.2 Power Spectrum

The relationships between the power spectrum $W(\omega)$ and the temporal ACF $B(\tau)$ can be written in terms of the Fourier transformation and the inverse Fourier transformation as

$$W_f(\omega) = \frac{1}{2\pi} \int_{-\infty}^{\infty} e^{-j\omega\tau} B_f(\tau) d\tau \quad (2.21)$$

and

$$B_f(\tau) = \int_{-\infty}^{\infty} e^{j\omega\tau} W_f(\omega) d\omega. \quad (2.22)$$

These two equations are known as the Wiener-Khinchine relationships. Inserting equation 2.22 into equation 2.18 gives a relationship between $D(\tau)$ and $W(\omega)$:

$$D_f(\tau) = 2 \int_{-\infty}^{\infty} [1 - \cos(\omega\tau)] W_f(\omega) d\omega. \quad (2.23)$$

Differentiation with respect to τ leads to expressions of $W_f(\omega)$ in terms of $D'_f(\tau)$ and $D''_f(\tau)$, respectively:

$$W_f(\omega) = \frac{1}{2\pi\omega} \int_0^{\infty} \sin(\omega\tau) D'_f(\tau) d\tau \quad (2.24)$$

and

$$W_f(\omega) = \frac{1}{2\pi\omega^2} \int_0^{\infty} \cos(\omega\tau) D''_f(\tau) d\tau. \quad (2.25)$$

2.2.3 Wavenumber Spectrum

Similar to the preceding section, the Wiener-Khinchine relationships between the one-dimensional wave-number spectrum along the x -direction $V_f(\kappa)$ and the spatial ACF $B_f(r)$ can be written:

$$V_f(\kappa) = \frac{1}{2\pi} \int_{-\infty}^{\infty} e^{-j\kappa r} B_f(r) dr \quad (2.26)$$

and

$$B_f(r) = \int_{-\infty}^{\infty} e^{j\kappa r} V_f(\kappa) d\kappa. \quad (2.27)$$

Inserting equation 2.27 into equation 2.20 gives a relationship between $D_f(r)$ and $V_f(\kappa)$:

$$D_f(r) = 2 \int_{-\infty}^{\infty} [1 - \cos(\kappa r)] V_f(\kappa) d\kappa. \quad (2.28)$$

Differentiation with respect to r leads to expressions of $V_f(\kappa)$ in terms of $D'_f(r)$ and $D''_f(r)$, respectively:

$$V_f(\kappa) = \frac{1}{2\pi\kappa} \int_0^{\infty} \sin(\kappa r) D'_f(r) dr \quad (2.29)$$

and

$$V_f(\kappa) = \frac{1}{2\pi\kappa^2} \int_0^{\infty} \cos(\kappa r) D''_f(r) dr. \quad (2.30)$$

2.2.4 Integral Scales and Spectral Widths

In Tatarskii (1971) [p.10], the integral time scale is defined as

$$\tau_i = \frac{1}{B_f(0)} \int_{-\infty}^{\infty} B_f(\tau) d\tau, \quad (2.31)$$

and the spectral width of the power spectrum is defined as

$$\omega_i = \frac{1}{W_f(0)} \int_{-\infty}^{\infty} W_f(\omega) d\omega \quad (2.32)$$

with the following relationship between the two:

$$\tau_i \omega_i = 2\pi. \quad (2.33)$$

For the integral length scale by means of the Taylor's Hypothesis we can write:

$$r_i = \frac{1}{B_f(0)} \int_{-\infty}^{\infty} B_f(r) dr \quad (2.34)$$

and for the spectral width of the wavenumber spectrum

$$\kappa_i = \frac{1}{V_f(0)} \int_{-\infty}^{\infty} V_f(\kappa) d\kappa \quad (2.35)$$

with the following relationship:

$$\kappa_i r_i = 2\pi. \quad (2.36)$$

2.2.5 Inertial Subrange and Structure Parameter

According to Kolmogorov (1941b) and Obukhov (1941) $D_f(r)$ is proportional to $r^{2/3}$ in the inertial subrange

$$D_f(r) = C_f^2 r^{2/3}, \quad (2.37)$$

where C_f^2 is referred to as the structure parameter of f . From the relationship between $V_f(\kappa)$ and $D_f(r)$ [Equation 2.29], we find

$$\begin{aligned} V_f(\kappa) &= \frac{1}{2\pi\kappa} \int_0^{\infty} \sin \kappa r \left[\frac{2}{3} C_f^2 r^{\frac{2}{3}-1} \right] dr \\ &= \frac{C_f^2}{3\pi\kappa} \int_0^{\infty} \sin(\kappa r) r^{\frac{2}{3}-1} dr \\ &= \frac{C_f^2}{3\pi\kappa} \kappa^{-\frac{2}{3}} \Gamma(2/3) \sin\left(\frac{\pi}{3}\right) \\ &= 0.1244 C_f^2 \kappa^{-\frac{5}{3}}. \end{aligned} \quad (2.38)$$

Taylor's hypothesis leads to a simple relationship between time lag and stream-wise spatial lag:

$$r = U\tau, \quad (2.39)$$

where U is the magnitude of the ensemble-averaged wind vector. Inserting into (2.37) gives

$$D_f(\tau) = C_f^2 U^{2/3} \tau^{2/3}. \quad (2.40)$$

From the relationship between $W_f(\omega)$ and $D'_f(\tau)$ [Equation 2.24], we find

$$\begin{aligned} W_f(\omega) &= \frac{1}{2\pi\omega} \int_0^\infty \sin \omega\tau \left[\frac{2}{3} C_f^2 U^{2/3} \tau^{\frac{2}{3}-1} \right] d\tau \\ &= \frac{C_f^2 U^{2/3}}{3\pi\omega} \int_0^\infty \sin(\omega\tau) \tau^{\frac{2}{3}-1} d\tau \\ &= \frac{C_f^2 U^{2/3}}{3\pi\omega} \omega^{-\frac{2}{3}} \Gamma(2/3) \sin\left(\frac{\pi}{3}\right) \\ &= 0.1244 C_f^2 U^{2/3} \omega^{-\frac{5}{3}}. \end{aligned} \quad (2.41)$$

It should be pointed out that equations 2.38 and 2.41 are integrals from zero to infinity over the *two-sided* spectrum $V_f(\kappa)$ and $W_f(\omega)$, respectively. Because $V_f(\kappa)$ and $W_f(\omega)$ are even functions, they can be rewritten as *one-sided* spectrum $F_f(\kappa)$ and $S_f(\omega)$ in terms of the two-sided spectrum, respectively:

$$F_f(\kappa) = 2V_f(\kappa) \quad (2.42)$$

and

$$S_f(\omega) = 2W_f(\omega), \quad (2.43)$$

where $F_f(\kappa)$ and $S_f(\omega)$ are zero for negative κ and ω , respectively. Then equations 2.38 and 2.41 can be written as

$$F_f(\kappa) = 0.2488 C_f^2 \kappa^{-\frac{5}{3}} \quad (2.44)$$

and

$$S_f(\omega) = 0.2488C_f^2U^{2/3}\omega^{-\frac{5}{3}}, \quad (2.45)$$

where equation [2.44] agrees with Muschinski et al. (2001) equation [9], if it is approximated as

$$F_f(\kappa) \approx 0.249C_f^2\kappa^{-\frac{5}{3}}. \quad (2.46)$$

2.2.6 Locally Isotropic Velocity Fields

For locally homogeneous and isotropic turbulent velocity fields, Kolmogorov (1941a) predicts a 4/3-ratio between the directional and the normal components in the inertial sub-range, as described by equation [21] of Kolmogorov (1941a):

$$\frac{[1 - R_{nn}(r)]}{[1 - R_{dd}(r)]} = \frac{4}{3} \quad (2.47)$$

where

$$R_{nn}(r) = \frac{B_{nn}(r)}{B_{nn}(0)} = \frac{B_{nn}(r)}{\sigma_{nn}^2} \quad (2.48)$$

is the correlation function of the velocity component in a direction normal (transverse) to the r -direction and

$$R_{dd}(r) = \frac{B_{dd}(r)}{B_{dd}(0)} = \frac{B_{dd}(r)}{\sigma_{dd}^2} \quad (2.49)$$

is the correlation function of the directional (or longitudinal) velocity component. Noting that the variance of the transverse component σ_{nn}^2 and that of the longitudinal component, σ_{dd}^2 must be equal for isotropy,

$$\sigma_{nn}^2 = \sigma_{dd}^2 \quad (2.50)$$

and that the correlation functions R_{nn} and R_{dd} are by definition 1 at a spatial lag $r = 0$,

$$R_{nn}(0) = R_{dd}(0) = 1, \quad (2.51)$$

equation [2.47] can be rewritten as:

$$\frac{\sigma_{nn}^2 [R_{nn}(0) - R_{nn}(r)]}{\sigma_{dd}^2 [R_{dd}(0) - R_{dd}(r)]} = \frac{4}{3}. \quad (2.52)$$

With equation [2.20] we find

$$\frac{D_{nn}(r)}{D_{dd}(r)} = \frac{4}{3}. \quad (2.53)$$

Inserting equation [2.37] into equation [2.53] a 4/3 ratio is also found for the structure parameters:

$$\frac{D_{nn}(r)}{D_{dd}(r)} = \frac{C_{nn}^2 r^{2/3}}{C_{dd}^2 r^{2/3}} = \frac{C_{nn}^2}{C_{dd}^2} = \frac{C_w^2}{C_u^2} = \frac{C_v^2}{C_u^2} = \frac{4}{3}, \quad (2.54)$$

where C_{nn}^2 is the structure parameter of the transversal vector component and C_{dd}^2 is the structure parameter of the longitudinal vector component. Here, C_u^2 is the structure parameter of the velocity vector component in the x -direction, and C_v^2 and C_w^2 are the structure parameters of the velocity components v and w , where v is the y -component of the velocity vector, and w is the z -component. In the following we assume the z -axis to point upward.

2.3 Monin-Obukhov Theory

Subsection 2.3.1 gives a definition of the atmospheric boundary layer and the surface layer. In subsection 2.3.2, the roughness length z_0 is defined. Equations for the turbulence fluxes (latent heat, sensible heat, momentum and temperature) are given in subsection 2.3.3. The turbulence scaling parameters, describing the intensity of turbulence, are defined in section 2.3.4. Section 2.3.5 introduces the stability conditions. Section 2.3.6 states the *logarithmic law of the wall*. Profile correction functions, as the central result of the Monin-Obukhov theory (generalization of the logarithmic law of the wall) are discussed in subsection 2.3.7.

2.3.1 Atmospheric Boundary and Surface Layer

Garratt (1992)[p.1] defines the atmospheric boundary layer (ABL) as “the layer of air directly above the Earth’s surface in which the effects of the surface (friction, heating, cooling) are felt directly on time scales less than a day and in which significant fluxes of momentum, heat or matter are carried by turbulent motions on a scale of the order of the depth of the boundary layer or less.”

The surface layer of the atmosphere, the lowest part of the ABL, is defined as the region in which turbulent fluxes may be assumed to be constant as a function of height and the effect of the Coriolis force due to the rotation of the earth can be neglected. The height of the surface layer is commonly defined as 10 % of the ABL height; see figure 2.2.

2.3.2 Roughness length

Another important parameter shown in figure 2.2 is the roughness length z_0 . The roughness length characterizes the surface structure and can have values from a fraction of a millimeters (smooth surface) to several meters (rough surface, trees, urban area). A quantitative definition of z_0 follows from the logarithmic law of the wall, see subsection 2.3.6.

2.3.3 Turbulence Fluxes

Since the momentum-flux, sensible heat-flux and latent heat flux are approximately constant in the surface layer (independent of height), the surface layer is also referred to as the constant flux layer. The momentum flux (also Reynolds stress) τ_r is given as

$$\tau_r = \rho_{air} \sqrt{\overline{u'w'^2} + \overline{v'w'^2}}, \quad (2.55)$$

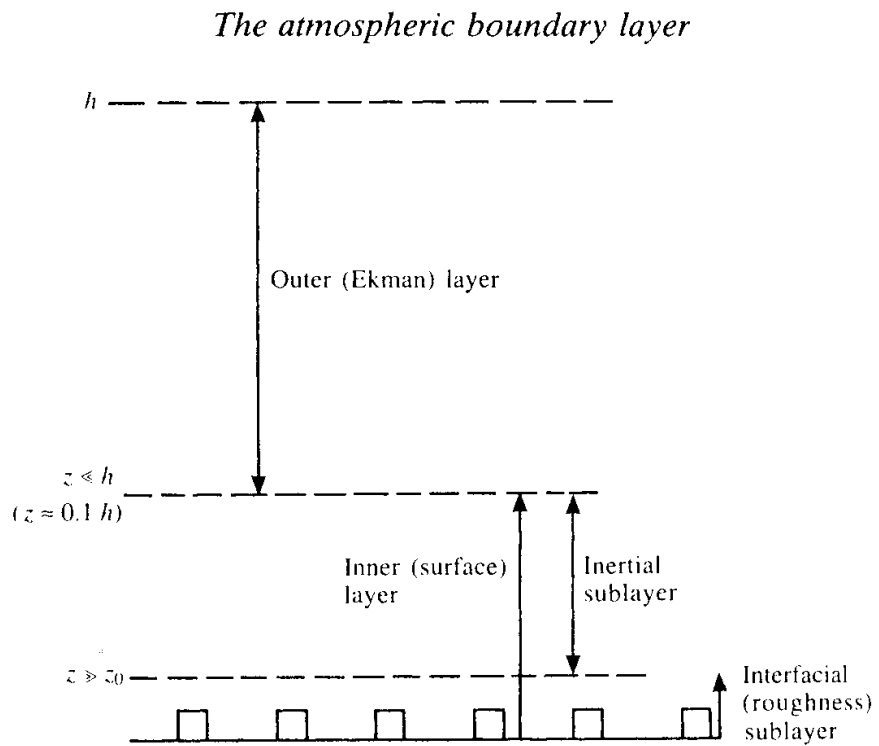


Figure 2.2. Structure of atmospheric boundary layer; from Garratt (1992)[p.2]

where $\overline{u'w'}$ is the covariance of the horizontal velocity u' with the vertical velocity w' and where $\overline{v'w'}$ is the covariance of the horizontal lateral velocity v' with w' . ρ_{air} is the density of air. The sensible heat flux H_S is given by

$$H_S = \rho_{air} c_p \overline{w'\theta'}, \quad (2.56)$$

where c_p is the specific heat capacity of air at constant pressure and $\overline{w'\theta'}$ is the covariance of w' with the temperature θ' . The latent heat flux is defined as

$$H_L = \lambda_w \overline{w'q'}, \quad (2.57)$$

where λ_w is the specific heat of vaporization of water, and $\overline{w'q'}$ the covariance of w' with the specific humidity q' . In addition, a temperature flux Q can be denoted as

$$Q = \frac{H_S}{\rho_{air} c_p} = \overline{w'\theta'}, \quad (2.58)$$

which is sometimes referred to as the kinematic heat flux.

2.3.4 Turbulence Scaling Parameters

The following four scaling parameters are defined for the surface layer. These are: velocity scale (also known as the friction velocity)

$$u_* = \sqrt{\frac{\tau_r}{\rho_{air}}} = (\overline{u'w'^2} + \overline{v'w'^2})^{1/4}, \quad (2.59)$$

the temperature scale

$$\theta_* = \frac{Q}{u_*} = \frac{\overline{w'\theta'}}{u_*} \quad (2.60)$$

the Monin-Obukhov length

$$L_* = -\frac{u_*^3 \bar{\theta}}{KgQ} = -\frac{u_*^3 \bar{\theta}}{Kg w' \theta'} = -\frac{\bar{\theta}}{Kg} \frac{u_*^2}{\theta_*} \quad (2.61)$$

and the height z AGL. $\bar{\theta}$ denotes the mean temperature in the surface layer, K the Karman constant and g is the constant of gravity.

2.3.5 Stability Conditions

Stability conditions can be divided into the cases of unstable, neutral and stable stratification. The dimensionless height $\frac{z}{L_*}$ gives a compact description of the three cases, in which $\frac{z}{L_*}$ gives negative values for unstable stratification, values approaching zero for neutral stratification and positive values for stable stratification.

2.3.6 Logarithmic Law of the Wall

Equation [13] in Monin and Obukhov (1954) states the gradient of the mean wind speed with respect to height z (mean wind speed height profile) near the surface as:

$$\frac{dU(z)}{dz} = \frac{u_*}{Kz}. \quad (2.62)$$

Similarly the gradient of the mean temperature with respect to height z (mean temperature height profile) can be written as:

$$\frac{d\bar{\theta}(z)}{dz} = \frac{\theta_*}{z}. \quad (2.63)$$

Integration of 2.62 and 2.63 with respect to height z leads to

$$U(z) = \frac{u_*}{K} \ln \left(\frac{z}{z_0} \right) \quad (2.64)$$

and

$$\bar{\theta}(z) = \theta_* \ln \left(\frac{z}{z_0} \right), \quad (2.65)$$

which are the logarithmic law of the wall. Here equation [2.64] is identical with equation [18] in Monin and Obukhov (1954). Equations [2.64] and [2.65] give the mean values of wind speed and temperature at a given height z .

2.3.7 Profile Correction Functions

In Monin and Obukhov (1954) equations [29'] and [30'] state a more general form of the equations [2.62] and [2.63] including all three possible density stratifications:

$$\frac{dU}{dz} = \frac{u_*}{Kz} \phi_1 \left(\frac{z}{L_*} \right) \quad (2.66)$$

and

$$\frac{d\bar{\theta}(z)}{dz} = \frac{\theta_*}{z} \phi_2 \left(\frac{z}{L_*} \right), \quad (2.67)$$

where ϕ_1 is the correction function of the height profile of the mean wind speed and ϕ_2 is the correction function of the height profile of the temperature. Thus the Monin-Obukhov theory is a generalization of the logarithmic law of the wall. Equations [2.66] and [2.67] can be integrated with respect to z and lead to the mean wind speed and temperature at a given height z respectively:

$$U(z) = \frac{u_*}{K} \left[\ln \left(\frac{z}{z_0} \right) - \Psi_1 \left(\frac{z}{L_*} \right) \right] \quad (2.68)$$

and

$$\bar{\theta}(z) - \bar{\theta}(z_0) = \frac{\theta_*}{K} \left[\ln \left(\frac{z}{z_0} \right) - \Psi_2 \left(\frac{z}{L_*} \right) \right], \quad (2.69)$$

where $\Psi_1\left(\frac{z}{L_*}\right)$ and $\Psi_2\left(\frac{z}{L_*}\right)$ are the correction functions for the integrated profiles, corresponding to ϕ_1 and ϕ_2 . From equation [3.34] [p. 53] in Garratt (1992) it can be seen that a relationship between Ψ and ϕ can be expressed as:

$$\Psi\left(\frac{z}{L_*}\right) = \int \left[1 - \phi\left(\frac{z}{L_*}\right)\right] d\left(\frac{z}{L_*}\right). \quad (2.70)$$

For small values of $\phi\left(\frac{z}{L_*}\right)$ an analytical form can be written as:

$$\phi\left(\frac{z}{L_*}\right) = 1 + \beta_1 \frac{z}{L_*}, \quad (2.71)$$

where β_1 is the coefficient of a power law expansion (neglecting terms of order higher than one) and equation [2.71] is identical to equation [42] in Monin and Obukhov (1954). Inserting equation [2.71] into equation [2.70] gives:

$$\Psi\left(\frac{z}{L_*}\right) = -\beta_1 \frac{z}{L_*}. \quad (2.72)$$

Inserting equation [2.72] into equation [2.68] and equation [2.69], results in equations for the mean wind velocity $U(z)$ and the mean temperature $\bar{\theta}(z)$ as given by equations [43a] and [43b] in Monin and Obukhov (1954) respectively:

$$U(z) = \frac{u_*}{K} \left[\ln\left(\frac{z}{z_0}\right) + \beta_1 \frac{z}{L_*} \right], \quad (2.73)$$

known as the log-linear wind law, and

$$\bar{\theta}(z) - \bar{\theta}(z_0) = \frac{\theta_*}{K} \left[\ln\left(\frac{z}{z_0}\right) + \beta_2 \frac{z}{L_*} \right], \quad (2.74)$$

where β_2 is another coefficient. Figure 2.3 shows qualitatively how the different stability conditions resulting from the density stratification impact the wind profile.

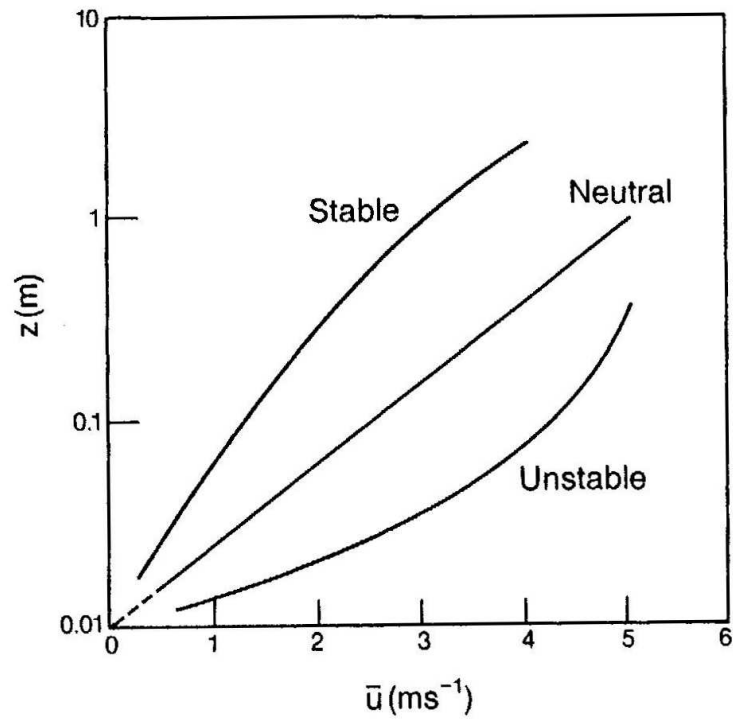


Figure 2.3. Wind profile in stable, neutral and unstable air; from Kaimal and Finnigan (1994) [p.12]

CHAPTER 3

SYSTEM DESCRIPTION

This chapter explains the system used for collection and storage of wind velocity, temperature and time stamps. The measurement principles of the sonic anemometer and thermometer are described in section 3.1. Followed by the explanation of the data logging system in section 3.2, which receives the data from the sonic, adds a time stamp and stores it, section 3.3 provides an analysis of the accuracy of the time stamps. In section 3.4 the format of the time stamps, data and the debug information is shown.

3.1 Sonic Anemometer and Thermometer Measurement Principle

The sonic anemometer relies on a simple and efficient measurement method, which will be summarized, based on Kaimal and Finnigan (1994)[p.247]. In the given sonic anemometer from R.M. Young Company (1999), three measurement paths of length d crossing through the same measurement volume from different directions are defined, as shown in figure 3.1. An ultrasonic transducer is placed at both ends of each of these paths. This transducer can send and receive an ultrasonic sound wave of a specific frequency, as seen in figure 3.2. The time t_1 for the ultrasonic sound wave to travel from one transducer to its counterpart can be stated as:

$$t_1 = \frac{d}{c - V_d}, \quad (3.1)$$



Figure 3.1. Sonic anemometer measurement paths and sample volume (Picture: R.M. Young Company (1999))

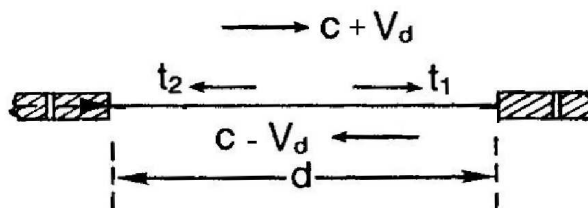


Figure 3.2. Ultrasonic transducer and measurement path from Kaimal and Finnigan (1994) [p.247]

where c is the speed of sound and V_d is the wind velocity along the measurement path. Similarly the time t_2 for an ultrasonic wave traveling in the opposite direction can be described as:

$$t_2 = \frac{d}{c + V_d}. \quad (3.2)$$

Equations [3.1] and [3.2] can be rewritten as:

$$c - V_d = \frac{d}{t_1} \quad (3.3)$$

and

$$c + V_d = \frac{d}{t_2}. \quad (3.4)$$

Subtracting equation [3.3] from [3.4] gives the wind velocity along the path as V_d :

$$V_d = \frac{d}{2} \left(\frac{1}{t_1} - \frac{1}{t_2} \right). \quad (3.5)$$

This gives the wind velocity V_d along the path d only in terms of the time t_1 , the time t_2 and the path length d . Note that for the sound velocity the following empirical equation exists:

$$c^2 = 403T \left(1 + 0.32 \frac{e}{p} \right), \quad (3.6)$$

where T is the air temperature (in K), e the water vapor pressure and p the air pressure. In Kaimal and Finnigan (1994) equation [3.6] is approximated as:

$$c^2 = 403T \left(1 + 0.32 \frac{e}{p} \right) \approx 403T \left(1 + 0.38 \frac{e}{p} \right) = 403T_v, \quad (3.7)$$

with T_v as the virtual temperature. Taking the sum of equation [3.3] and [3.4] results into:

$$\frac{2c}{d} = \frac{1}{t_1} + \frac{1}{t_2}. \quad (3.8)$$

Equation [3.8] can be rewritten as

$$c = \frac{d}{2} \left(\frac{1}{t_1} + \frac{1}{t_2} \right) \quad (3.9)$$

or

$$c^2 = \frac{d^2}{4} \left(\frac{1}{t_1} + \frac{1}{t_2} \right)^2. \quad (3.10)$$

Equating equation [3.7] and equation [3.10] gives:

$$T_v = \frac{d^2}{1612} \left(\frac{1}{t_1} - \frac{1}{t_2} \right)^2, \quad (3.11)$$

which is, again, only in terms of the of the time t_1 , the time t_2 and the path length d . This shows that measuring the travel times t_1 and t_2 is sufficient to compute the wind vector components and the virtual temperature. In the given sonic this is done by a micro-controller integrated into the sonic, which measures the transition times, applies several corrections (e.g. wake, cross wind, transducer shadowing) and computes the wind vector components and the virtual temperature. This data is then provided through a serial asynchronous RS232 interface.

3.2 Data Logging System

The serial interface of the sonic described in subsection 3.1 was connected to a serial-to-universal serial bus (USB) converter for each of the two sonics used. And these were attached to a standard notebook computer running Linux.

In Linux any hardware or software device or data unit is represented by a file. In the case of the serial ports provided via the USB port these files are `/dev/ttyUSB0` and `/dev/ttyUSB1` respectively. In this way the interaction with these devices is provided in a similar way as interaction is provided with data units (normal files). So for data units the main actions are

Allocate program variables and resources		
Open file descriptors (FD) devices to sonic 1 and 2		
Clear and initial new FD settings		
Save old serial port settings		
Initial new serial port settings		
Write new FD and serial port settings		
Open files for data and time stamps storage		
Wait for a dummy read from sonic 1		
Wait for a dummy read from sonic 2		
For index=0 to infinity		
Active Sonic ?	Sonic 1	Sonic 2
Read data	Read data	Read data
Read time stamp	Read time stamp	Read time stamp
Write time stamp	Write time stamp	Write time stamp
Write data	Write data	Write data
Clear sonic 1	Clear sonic 2	Clear sonic 2
Activate sonic 2	Activate sonic 1	Activate sonic 1

Figure 3.3. Program structure of data logging program

to read or write data or to seek a position. For devices another action is possible, this action is the configuration of the device (also called setup control or initialization). This action usually specifies the way the device operates (e.g. how it handles data). However once this phase is finished, the device can be treated very similar to a data unit.

In figure 3.3, the logical flow of the data logging and time stamping program is shown, starting with allocating variables and other resources needed. The second step is to open the serial port devices using a file descriptor (FD) list. A FD in this concept is essentially a program internal universal pointer to any device file. This FD-list is essential for defining a set of devices. Once opened, these FD's are reset to a defined state by emptying their buffers, in step three. As the next step the old configuration of the serial port is saved as a precaution and for step five the new desired configuration of the serial ports is assigned to variables. As step six the configurations of the FD's and the serial ports are written, which concludes the setup process.

Now, as the devices are ready to be read, the program does a dummy read on each of the two devices, disregards this data received and clears the buffer. This action ensures that the program is now synchronized with the sonics and does not receive incomplete data messages. As of this point the second sonic was the last device read and the first sonic is assumed to provide data next (to be set active in the FD list). Once the activity signal is detected, the data is read from the device and a time stamp is generated. Both are then stored in the data unit. The final step before getting ready to receive data again is now to clear the device again and to activate the second sonic, which is expected to receive data next.

Then the whole process is repeated for the second sonic by receiving data, creating the time stamp, storing data and time stamp and switches back to the first sonic. This process, known as ping-pong technique, continues until an interruption signal is given by sending CTRL-C to the program. After this signal, a signal handler will be called. This is the only way to exit the infinite loop. The signal handler then closes the data units, restores the old

serial port configurations and terminates the program.

Note that this last step is not shown in figure 3.3, since it is not part of the main program, but merely a way to terminate the data logger correctly at any given time.

3.3 Time Stamp Validation

Section 3.2 pointed out that not only the data but also time stamps associated with the data are stored. It is important to determine the validity of these time stamps, and whether they are a reliable representation of time. Ideally the time stamps should be equidistant in time, resulting in a linear increase of recorded time as a function of the time-stamp index. In the case of interleaved timestamps from two sensor data streams (as it is the case for the two sonics), the offset between the time stamps with even and odd index should be constant, which implies that the sampling rates of the two sensors are *exactly* identical (e.g derived from the same reference oscillator). This furthermore assumes that the time for both sonics from measurement of the data till time stamp generation and storage is constant.

For the further analysis a few terms have to be defined, which are *raw time stamp*, *corrected time stamp* and *linear time stamp*. Note that the time stamp is originally created as described in section 3.4 for every data point. For the following analysis the time stamps are converted to seconds counted from the beginning of the experiment. This procedure simplifies the analysis significantly.

The simplest time stamp is a raw time stamp, which is the time stamp as it is stored by the data logging system. In figure 3.4 in the upper and center diagram the first hundred raw time stamps for the first and the second sonic are plotted as solid lines against their index. The spikes shown in these time stamps are caused by an operating system adjusting mechanism, which tries to compensate for the PC-clock drift.

A corrected time stamp means that an algorithm has checked whether the time between two consecutive samples is an integer number multiple of the sampling interval or not. In the

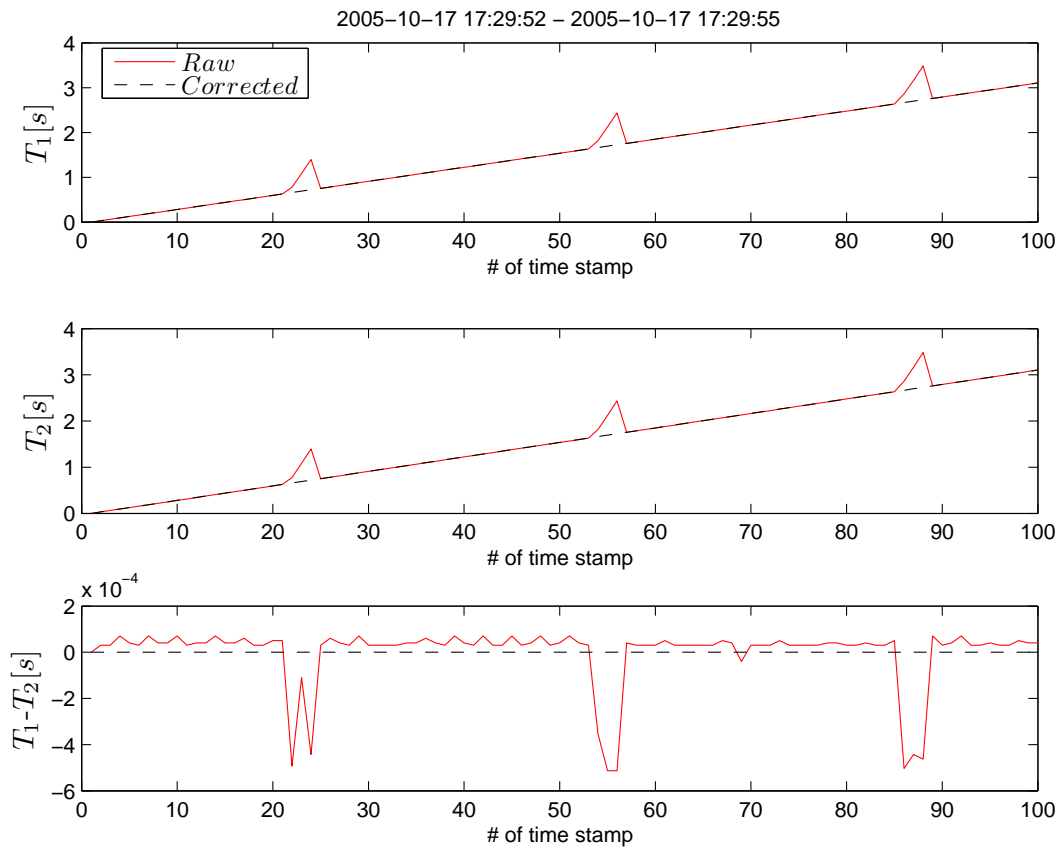


Figure 3.4. Raw and corrected time stamps from sonic 1 and 2 data and time difference over a time of 4s.

case of a negative result, the erroneous time stamp will be corrected by replacing it with the directly preceding time stamp plus the nearest integer number multiple of the sampling interval. Note that this algorithm allows for a small correct range around the integer number multiple of the sampling interval for the time between samples, rather than one value. This is needed because there is always small jitter in the time stamping interval. Therefore this method does not correct for any drift and might contain jumps in time because it checks for the integer multiple of the sampling interval, rather than for the sampling interval. In figure 3.4 the dashed line shows the corrected time stamps corresponding to the raw time stamps plotted against their index. It can be seen that spikes from the raw time stamps were successfully removed.

Linear time stamping means that the time stamps are recomputed by taking the last and the first time stamp from the whole data set, and that a linear estimation between them is computed. Then all values between the first and the last time stamp are replaced. Note that use of this technique can introduce additional errors compared to the true time if the original time series contains a drift. Otherwise the resulting time stamps will be perfect, as missing samples are assumed not to exist.

The bottom diagram of figure 3.4 shows the differences between the two sonics for the raw and for the corrected time stamps. It can be seen that the difference of the corrected time stamp is close to zero and that the difference between raw time stamps is a small value compared to the sampling interval. For the latter one, however, this small offset is increased when the clock adjustment spike is observed. This seems to be the case because the clock is adjusted much faster than normally. However, even this increased offset is small compared to the time between time stamps, so that no large relative error is generated between time stamps of both sonics.

Since figure 3.4 only shows a very small time period, not all possible errors might have occurred. Figure 3.5 shows the relative error between the sonics for all three available time stamps over the total experiment time. It can be seen that there are many spikes in the

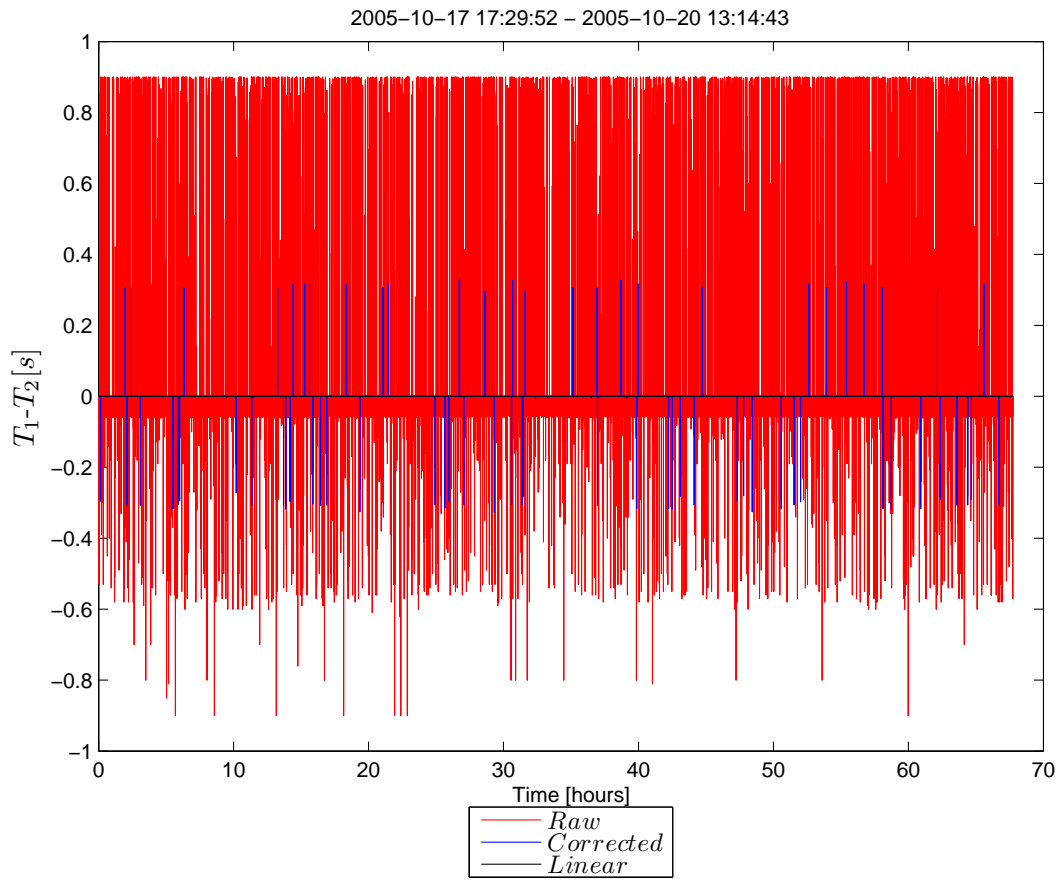


Figure 3.5. Relative error between both sonics for linear, corrected and raw timestamps.

raw time stamps, significantly reduced number of spikes in the corrected time stamps and none in the linear time stamps. Assuming that few spikes in the corrected time stamps are caused by missing samples, it can be justified to assume that most of the data shown has no missing samples. Based under this assumption the problem of ignoring missing samples, when using the linear time stamps, should be negligible.

Here two more possible errors are explained. Note that all effects are superimposed on

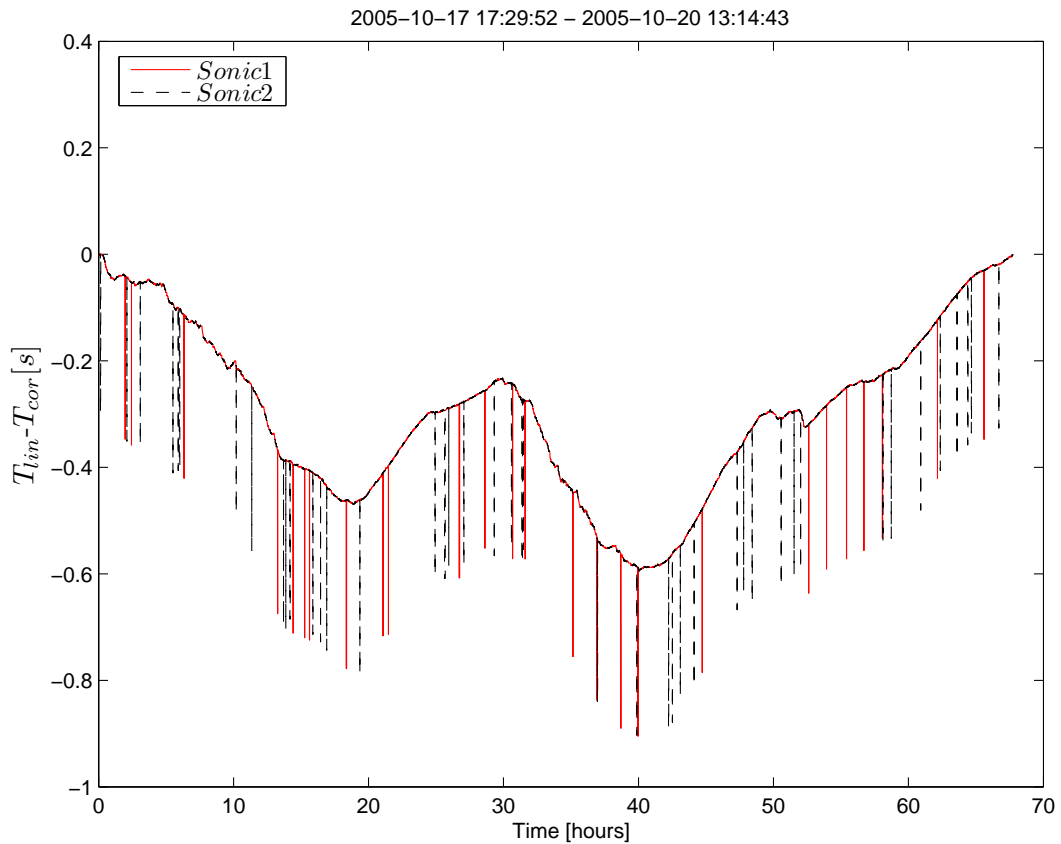


Figure 3.6. Drift of PC clock over 66 h.

each other. One of the additional errors, which can appear if two sonics are not referenced to the same oscillator (the sampling frequencies might not be exactly the same), is that a phase error can accumulate. This can switch the order of sampling of the sonics with respect to each other. Thus the data logging program described in section 3.2 will lose one data point, since it expects a value from the other sonic to be sent. However this error can

be tracked by finding the difference between two consecutive samples, and detect, when the difference is twice the sampling interval. Note that this error still assumes a perfect PC-clock oscillator.

The PC-clock oscillator drifts in general due to temperature changes. In figure 3.6 such a drift is shown for the whole experiment time period. Figure 3.6 shows the difference between the corrected time stamps and the linear time stamps. Interestingly, a kind of diurnal cycle can be seen in the drift, which confirms the dependency of the time stamp drift with temperature. The spikes are likely resulting from missing samples, as explained before. Note that the drift of the PC-clock over the experiment time is on the order of a second.

When using the two sonics alone with the same computer as a data logger, it can also be seen that the relative time between the two sonics is stable. But the drift might become a problem in reference to external systems.

3.4 File Format

The data and the time stamps are stored to a data unit on a mass storage device. The data unit is a plain text file (also known as ASCII file). The two files containing the two data stream from sonic 1 and 2 are named *SONIC_1_20051017205809.DAT* and *SONIC_2_20051017205809.DAT*, respectively. The time stamp included in the filename is the start time, day, month and year of the data record.

The files contain, for each text line in this order, a time stamp, as shown in table 3.1, the data as shown in table 3.2 and debugging information, as shown in table 3.3. Note that for the main data set used in the data analysis (20051017T175952 eastern daylight time (EDT) to 20051020T115952 EDT) only the bold type values were recorded, to reduce the file size.

Year	Month	Day	Hour	Minute	Seconds
2005	07	20	14	31	15.355233

Table 3.1. Time stamp format

u	v	w	Azimuth	Elevation	3d-Speed	Speed of Sound	Temperature
$[\frac{m}{s}]$	$[\frac{m}{s}]$	$[\frac{m}{s}]$	$[^{\circ}]$	$[^{\circ}]$	$[\frac{m}{s}]$	$[\frac{m}{s}]$	$[^{\circ}C]$
-0.86	0.16	-0.20	281.0	-12.9	0.91	349.84	30.57

Table 3.2. Data format

Error Flag	Internal Voltage
0	26.5

Table 3.3. Debug information

CHAPTER 4

EXPERIMENT SETUP AND DATA ANALYSIS

4.1 Experiment Location and Setup

To test the turbulence measurement system described in the preceding chapter, an experiment was performed at the Tilson farm facility of the Microwave Remote Sensing Lab in Amherst, MA. Timestamps, temperatures and the three wind vector components were recorded for both of the sonics from the 17th of October 2005 at 17:29:52 eastern daylight time (EDT) until the 20th of October 2005 at 13:14:42 EDT.

Figures 4.1 and 4.2 show the setup of the sonics on top of standard light stand tripods. The sonics were stabilized using nylon strings attached to the sonic frame and to tent pegs in the ground. The measurement height was $z_1 = 3.8$ m for one sonic and $z_2 = 3.0$ m for the other. The centers of the tripod bases were separated by $d = 1.8$ m. It should be noted that this was only a tentative setup, since the two professional 20-foot meteorological tripods ordered were not available in time. In the future, the professional system will be used because it is more robust, allows larger measurement heights and can facilitate multiple sensors on a single tower.

4.2 Weather Conditions

Another factor influencing the data is the weather. Analysis of the cloud coverage information from www.weather.com for the given time period from the 17th of October



Figure 4.1. Experiment setup at Tilson farm facility (Picture: Yonghun Cheon)



Figure 4.2. Close up of sonics (Picture: Yonghun Cheon)

2005 at 17:29:52 EDT till the 20th of October 2005 at 13:14:42 EDT, shows that it was between cloudy, mostly cloudy and sometimes partly cloudy. There was no precipitation.

4.3 Coordinate Systems

The sonic can be set to provide the wind vector components u (horizontal), v (lateral) and w (upward) in a rectangular coordinate system referenced to its frame, as shown in figure 4.3. However the most useful coordinate system for the application of turbulence theory is a stream-wise one, since it allows for simplification of the theory. In the rectangular stream-wise coordinate system the unit vector of the wind component u is the unit vector of the mean wind vector. The data is converted from the sonic coordinate system to the stream-wise coordinate system by rotation, which is described in subsection 4.4.3.

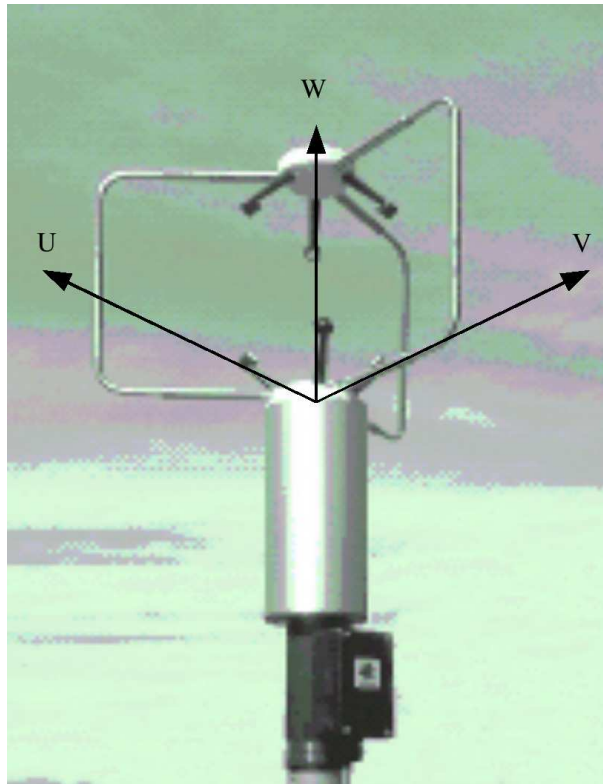


Figure 4.3. Sonic coordinate system (Picture: R.M. Young Company (1999))

4.4 Data Preparation

4.4.1 Raw Data

Raw atmospheric data can be written in the form of a mean quantity \bar{f} plus a fluctuating part f' , also known as Reynolds notation:

$$f = \bar{f} + f'. \quad (4.1)$$

For a wind vector decomposed into the rectangular sonic coordinate system the resulting equations are shown in table 4.1.

Wind vector component	Total Component	Mean
horizontal	$u = \bar{u} + u'$	$\bar{u} = \frac{1}{N} \sum_{i=1}^N u_i$
horizontal lateral	$v = \bar{v} + v'$	$\bar{v} = \frac{1}{N} \sum_{i=1}^N v_i$
vertical upward	$w = \bar{w} + w'$	$\bar{w} = \frac{1}{N} \sum_{i=1}^N w_i$

Table 4.1. Wind vector components in Reynolds notation

4.4.2 Averaging Interval

To resolve mean quantities of velocity and temperature, an averaging interval has to be chosen. It has to take two important parameter into account. First of which is the variance of the wind fluctuation around the mean. The second one is the time scale of the diurnal cycle, which is 24 hours, but can have significant changes on the order of hours. As a part of the Reynolds notation in table 4.1, the mean value of a stationary random time function $f(t)$ was estimated as time average $\bar{f}(t)$ instead of ensemble average $\langle f(t) \rangle$. However if a time average is taken over a long enough time, it converges to the ensemble average $\langle f(t) \rangle$:

$$\bar{f}(t) = \langle f(t) \rangle = \lim_{N \rightarrow \infty} \frac{1}{NT_s} \sum_{i=1}^N f(iT_s), \quad (4.2)$$

where T_s is the sampling interval, i is the sample number and N the total numbers of samples taken into account. Using an infinite sum of a time series however is impractical and the law of large numbers allows for truncating of this sum if the number of averaged independent samples $N_{ind} = \frac{T}{\tau_i}$ is large. Here τ_i is the integral time scale defined in equation [2.31] and $T = NT_s$ is the total time taken into account for the calculation or simple averaging time. A sample is called independent in this context if it is spaced further then the integral time scale τ_i away from the preceding sample. In other words, a sample is dependent on a preceding sample, if the spacing between them is less then the integral time scale τ_i .

In order to obtain a large number of independent samples, the averaging time T therefore must be much larger then the integral time scale τ_i :

$$T \gg \tau_i. \quad (4.3)$$

The law of large numbers can be written as:

$$\sigma_f^2 = \frac{\tau_i}{T} \sigma_f^2, \quad (4.4)$$

where σ_f^2 is the variance of the time average (with the averaging time T). To get a realistic understanding of the range of expected reduction of the variance of the estimation of the mean value of the velocity or temperature, real data has to be inserted into equation [4.4]. From velocity measurements shown later in section 4.5 the variance for one given time series was estimated as $\sigma_u^2 = 1.20(\frac{m}{s})^2$ and the integral time scale was estimated as $\tau_i \approx 5s$. Note that the averaging time is a value which has to be a trade-off between two demands. First there is the demand for a larger averaging time to reduce the variance of the estimation of mean values. On the other hand, we assume stationarity, which does not hold for longer averaging times, which are a significant fraction of the diurnal cycle. In Kaimal and Finnigan (1994) [p.256] a maximum averaging time is suggested as about as

$T \approx 3600s$, used in the following estimations. Inserting these values gives the standard deviation $\sigma_{\bar{u}}$ of the stationary random time function of the velocity component u as:

$$\sigma_{\bar{u}} = \sqrt{\frac{\tau_i}{T}} \sigma_u = \sqrt{\frac{5s}{3600s} 1.20 \left(\frac{m}{s}\right)^2} = 0.041 \frac{m}{s} \quad (4.5)$$

Another way to express this relationship is by the number of independent samples, which can be calculated for the given example as:

$$N_{ind} = \frac{T}{\tau_i} = \frac{3600s}{5s} = 720. \quad (4.6)$$

Table 4.2 gives results for the number of independent samples and accuracies for different averaging periods and a fixed integral time scale. As seen here, the user of the data has to decided, what is an acceptable $\sigma_{\bar{u}}$, which then sets the required averaging time.

Averaging Time [s]	# of Independent Samples	$\sigma_{\bar{u}}$ in % of σ_u
60	12	28.9
600	120	20.4
3600	720	3.7

Table 4.2. Number of independent samples and accuracy for integral time scale $\tau_i = 5s$

4.4.3 Data Rotation

In section 4.3 the sonic- and stream-wise coordinate systems were introduced. One commonly used method to convert data from the sonic- to the stream-wise coordinate system is the three-angle-rotation, which is described in Wilczak et al. (2001) and summarized here. Figure 4.4 shows a visualization of the rotations involved. The first step is to deter-

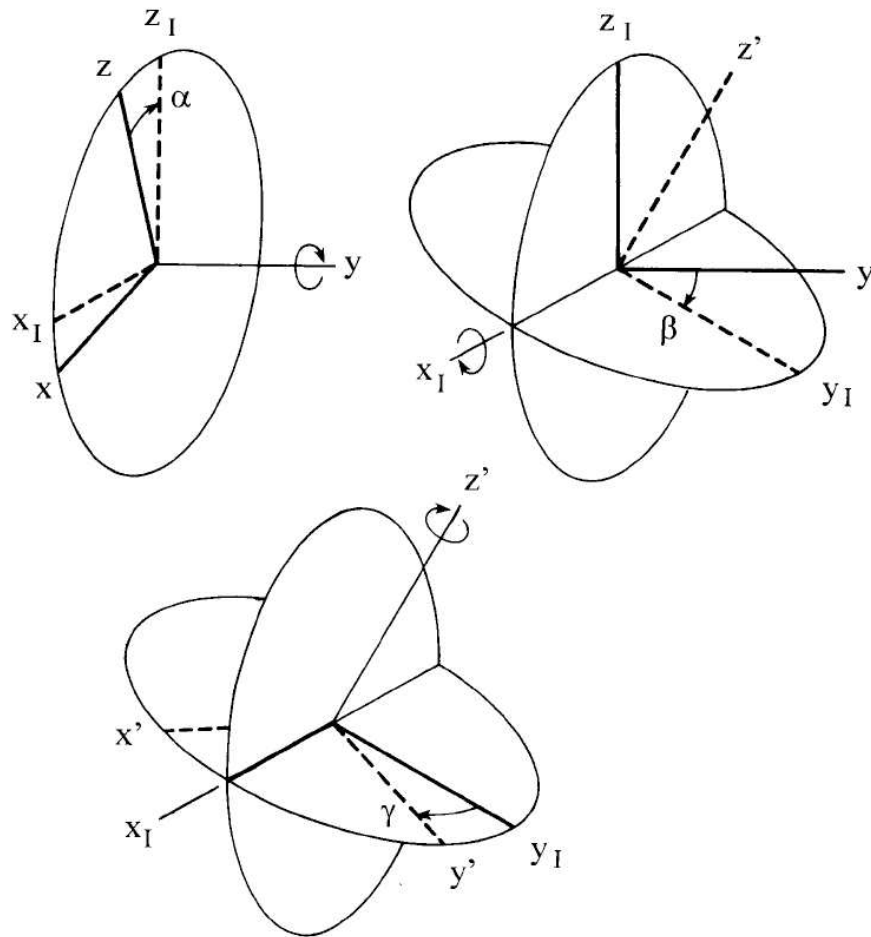


Figure 4.4. Three angle rotation method; diagram from Wilczak et al. (2001)

mine the angle α from the mean wind component \bar{u} in the x -direction and the mean wind component \bar{w} in the z -direction:

$$\alpha = \arctan\left(\frac{\bar{w}}{\bar{u}}\right). \quad (4.7)$$

The angle α can be used to compute the rotation matrix B :

$$B = \begin{bmatrix} \cos(\alpha) & 0 & \sin(\alpha) \\ 0 & 1 & 0 \\ -\sin(\alpha) & 0 & \cos(\alpha) \end{bmatrix}, \quad (4.8)$$

which converts the raw wind vector component u into the intermediate wind vector component u_I in the intermediate X_I -direction and the raw wind vector component w into the intermediate wind vector component w_I in the intermediate Z_I -direction:

$$\begin{bmatrix} u_I \\ v \\ w_I \end{bmatrix} = B \begin{bmatrix} u \\ v \\ w \end{bmatrix}, \quad (4.9)$$

Note that the raw wind vector component v was not effected by this step. This operation has now corrected the pitch, the next step is to compute the angle β to correct the roll angle:

$$\beta = \arctan\left(\frac{-\bar{w}_I}{\bar{v}}\right), \quad (4.10)$$

where \bar{w}_I is the mean of the intermediate wind vector component w_I . Following the rotation matrix C can be computed:

$$C = \begin{bmatrix} 1 & 0 & 0 \\ 0 & \cos(\beta) & -\sin(\beta) \\ 0 & \sin(\alpha) & \cos(\beta) \end{bmatrix}. \quad (4.11)$$

and applied similar to the rotation matrix B:

$$\begin{bmatrix} u_I \\ v_I \\ w' \end{bmatrix} = C \begin{bmatrix} u_I \\ v \\ w_I \end{bmatrix}, \quad (4.12)$$

which left u_I unchanged and converted the raw wind vector component v into the intermediate wind vector component v_I in the Y_I -direction and the intermediate wind vector component w_I into the final wind vector component w' in the Z' -direction in the stream-wise coordinate system. Finally the yaw angle γ can be computed from the mean of the intermediate wind vector component v_I and from the mean of the intermediate wind vector component u_I by using

$$\gamma = \arctan\left(\frac{\bar{u}_I}{\bar{v}_I}\right). \quad (4.13)$$

The third rotation matrix can then be found by using

$$D = \begin{bmatrix} \cos(\gamma) & -\sin(\gamma) & 0 \\ \sin(\gamma) & \cos(\gamma) & 0 \\ 0 & 0 & 1 \end{bmatrix}. \quad (4.14)$$

Applying matrix D then gives the two missing final wind vector components u' in the X' -direction and v' in the Y' -direction respectively:

$$\begin{bmatrix} u' \\ v' \\ w' \end{bmatrix} = D \begin{bmatrix} u_I \\ v_I \\ w' \end{bmatrix}. \quad (4.15)$$

Note that in this subsection the primed notation was only used to be consistent with the figure and Wilczak et al. (2001). To avoid confusion with the fluctuating parts, the wind vector components are redefined as:

$$\begin{bmatrix} u_{rot} \\ v_{rot} \\ w_{rot} \end{bmatrix} = \begin{bmatrix} u' \\ v' \\ w' \end{bmatrix}. \quad (4.16)$$

4.4.4 Data Detrending

However the rotation procedure is not sufficient to prepare the data for an analysis using the auto covariance function since it does not remove the mean value from the u_{rot} -component. It also ignores any possible trend in all three wind vector quantities u_{rot} , v_{rot} and w_{rot} . Therefore a detrending procedure has to be applied. This is done by fitting a linear function through the data:

$$y_{fit} = ax + b, \quad (4.17)$$

where a is the slope of the function fitted through the data and b is the y -intercept. Here, x is a variable, such as time, and y_{fit} is a variable depending on x , which can be any of the velocity components or the temperature. The constants a and b can be determined as

$$a = \frac{N \sum_{i=1}^N x_i y_i - \left(\sum_{i=1}^N x_i \right) \left(\sum_{i=1}^N y_i \right)}{N \sum_{i=1}^N x_i^2 - \left(\sum_{i=1}^N x_i \right)^2} \quad (4.18)$$

and

$$b = \frac{\left(\sum_{i=1}^N x_i^2 \right) \left(\sum_{i=1}^N y_i \right) - \left(\sum_{i=1}^N x_i \right) \left(\sum_{i=1}^N x_i y_i \right)}{N \sum_{i=1}^N x_i^2 - \left(\sum_{i=1}^N x_i \right)^2}, \quad (4.19)$$

where N is the number of points of the original data, i is the index of a point in the original data, x_i is the x -value of a point with the index i in the original data and y_i is the y -value of a point with the index i in the original data. The original data can be described as

$$y_i = f(x_i), \quad (4.20)$$

with

$$i = 1, 2, 3, \dots, N, \quad (4.21)$$

where $f()$ means *function of*. The function y_{fit} has now to be subtracted from the original function yielding a detrended function:

$$y_{det_i} = f(x_i) - [ax_i + b]. \quad (4.22)$$

4.4.5 Example for Raw, Rotated and Detrended Time Series

To illustrate the effects of rotation and detrending on the wind vector components u , v and w , a 35 min time series is shown as an example in figure 4.5. In figure 4.5 the diagrams in the left column show the raw time series. The center column displays the rotated time series and the right column contain first rotated and then detrended time series. The time series from the top to bottom are u , v and w , respectively. Looking at the diagrams on the left hand side, it can be seen that u and v are varying more strongly than w . The center diagrams show that the rotation concept can also be seen as transferring the mean parts of v and w to the u component. The over-plotted lines in these diagrams are the linear regression lines used to detrend data. It can be seen that there is a slight upward trend, even if the mean is zero as shown for v and w . In the three diagrams on the right only the fluctuating parts are left, since the rotation and then detrending was applied, so that the linear trend is eliminated and the mean value is zero.

4.5 Data Analysis

This section will analyze and describe the data from several perspectives. First, the noise level and the measurement errors are estimated, in subsections 4.5.1 and 4.5.2 respectively, to provide an understanding of the precision of the data. The second step is the

2005-07-20 15:41:15 – 2005-07-20 16:16:15

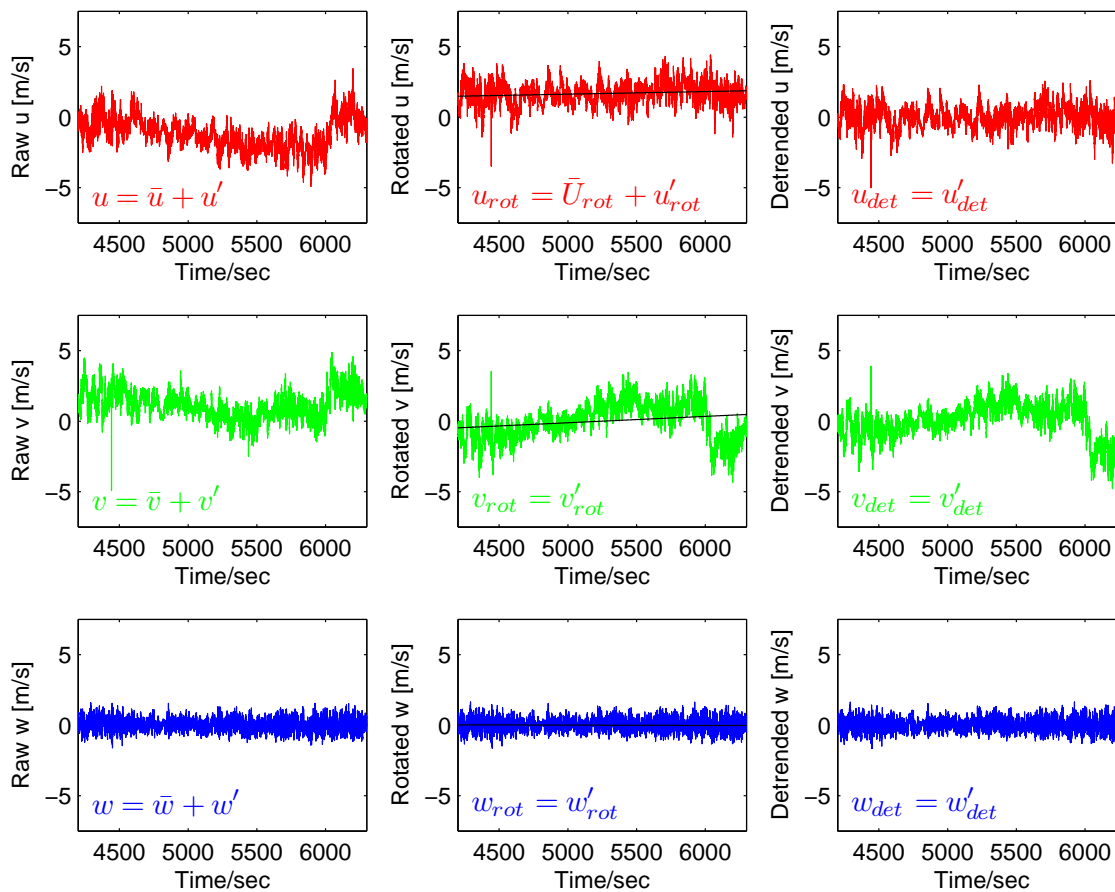


Figure 4.5. Wind vector components for a 35 min time series block (left column - raw), (center column - rotated), (right column - detrended)

time-domain analysis using the autocovariance function and the structure function in subsection 4.5.3. Subsection 4.5.4 presents a spectral viewpoint by means of the periodogram and the power spectrum. Based on the time and spectral domain analysis, subsection 4.5.5 shows the inertial subrange and presents the velocity and temperature structure parameter. In subsection 4.5.6 the integral length and time scales are resolved and discussed. The final subsection 4.5.7 shows the approach of isotropic behavior based on structure function and power spectrum.

4.5.1 Noise Estimation

A measured time series $m(t)$ can be described as a superposition of a true time series $f(t)$ and a noise component $n(t)$:

$$m(t) = f(t) + n(t). \quad (4.23)$$

Assuming that the noise $n(t)$ is zero-mean and uncorrelated, its ACF becomes:

$$B_n(\tau) = \begin{cases} \sigma_n^2 & : \tau = 0 \\ 0 & : \tau \neq 0 \end{cases} \quad (4.24)$$

Here σ_n^2 is the noise variance. Now considering the ACF of $m(t)$:

$$B_m(\tau) = \langle [f(t) + n(t)][f(t+\tau) + n(t+\tau)] \rangle = \langle f(t) + f(t+\tau) \rangle + \langle n(t) + n(t+\tau) \rangle, \quad (4.25)$$

where statistical independence is assumed, such that:

$$\langle f(t_1)n(t_2) \rangle = 0 \quad (4.26)$$

for any t_1 and t_2 . Therefore

$$B_m(\tau) = B_f(\tau) + B_n(\tau). \quad (4.27)$$

Now, considering the difference between $B_m(0)$ and $B_m(\tau)$:

$$B_m(0) - B_m(\tau) = B_f(0) + \sigma_n^2 - [B_f(\tau) + 0] = B_f(0) - B_f(\tau) + \sigma_n^2, \quad (4.28)$$

or

$$\Delta B_m(\tau) = \Delta B_f(\tau) + \sigma_n^2, \quad (4.29)$$

where

$$\Delta B_m(\tau) \equiv B_m(0) - B_m(\tau), \quad (4.30)$$

and

$$\Delta B_f(\tau) \equiv B_f(0) - B_f(\tau). \quad (4.31)$$

If $\tau \ll \tau_i$, then $\Delta B_f(\tau)$ may or may not be negligible compared to σ_n^2 . If $\Delta B_f(\tau)$ negligible, then equation [4.29] reduces to

$$\sigma_n^2 \approx \Delta B_m(\tau). \quad (4.32)$$

In many cases $\Delta B_f(\tau)$, however, may not be neglected. Using equation [2.18] $\Delta B_f(\tau)$ can then be written in terms of the structure function:

$$\Delta B_f(\tau) = \frac{1}{2} D_f(\tau). \quad (4.33)$$

If τ is in the inertial subrange, equation [2.40] can be inserted into equation [4.33], which gives the following result:

$$\Delta B_f(\tau) = \frac{1}{2} C_f^2 U^{2/3} \tau^{2/3}. \quad (4.34)$$

Inserting equation [4.34] into equation [4.29] gives:

$$\sigma_n^2 = \Delta B_m(\tau) - \frac{1}{2}C_f^2 U^{2/3} \tau^{2/3}, \quad (4.35)$$

valid only for the inertial subrange. For sonic anemometer, an effect known as spatial averaging smooths out all variations, which are smaller than the measurement path d . Correspondingly, a range of time lags can be determined using Taylor's hypothesis in which the ACF will be low-pass filtered:

$$\tau_{spat} \leq \frac{d}{\bar{U}} = \frac{0.15\text{m}}{1.84\frac{\text{m}}{\text{s}}} = 0.082\text{s}, \quad (4.36)$$

where $d = 0.15$ m was found from R.M. Young Company (1999) and $\bar{U} = 1.84\frac{\text{m}}{\text{s}}$ was computed from the time series of the velocity component u from data set 2005-10-18 16:29:52 EDT to 2005-10-18 17:29:52 EDT. Figure 4.6 shows the ACF's of the velocity components u, v, w and the temperature θ in the vicinity of the zero lag for the corresponding time. Only the ACF of the temperature shows a spike at the zeroth lag. Looking to the corresponding detrended temperature time series in figure 4.7 shows that the temperature fluctuation during this measurement period were in the same range as the precision of ± 0.1 K for the temperature measurements.

For the velocity data, however, during the whole experiment the fluctuation were many times larger than the precision of about $\pm 0.05\frac{\text{m}}{\text{s}}$ given by R.M. Young Company (1999) for velocity, so that a noise spike could not be found. Figure 4.8 shows these velocity fluctuation correspondingly to the temperature fluctuation of figure 4.7. The noise in the temperature data can be estimated by using equation [4.32] as

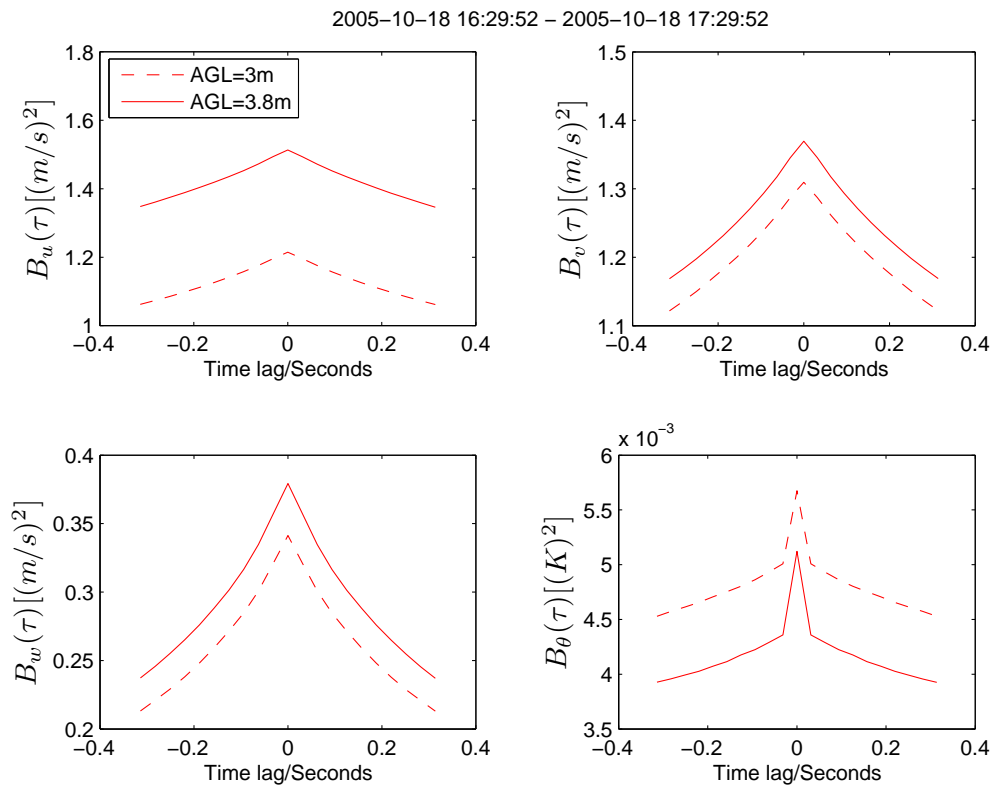


Figure 4.6. ACF of u, v, w and θ for maximum time lag $\tau = 0.32s$

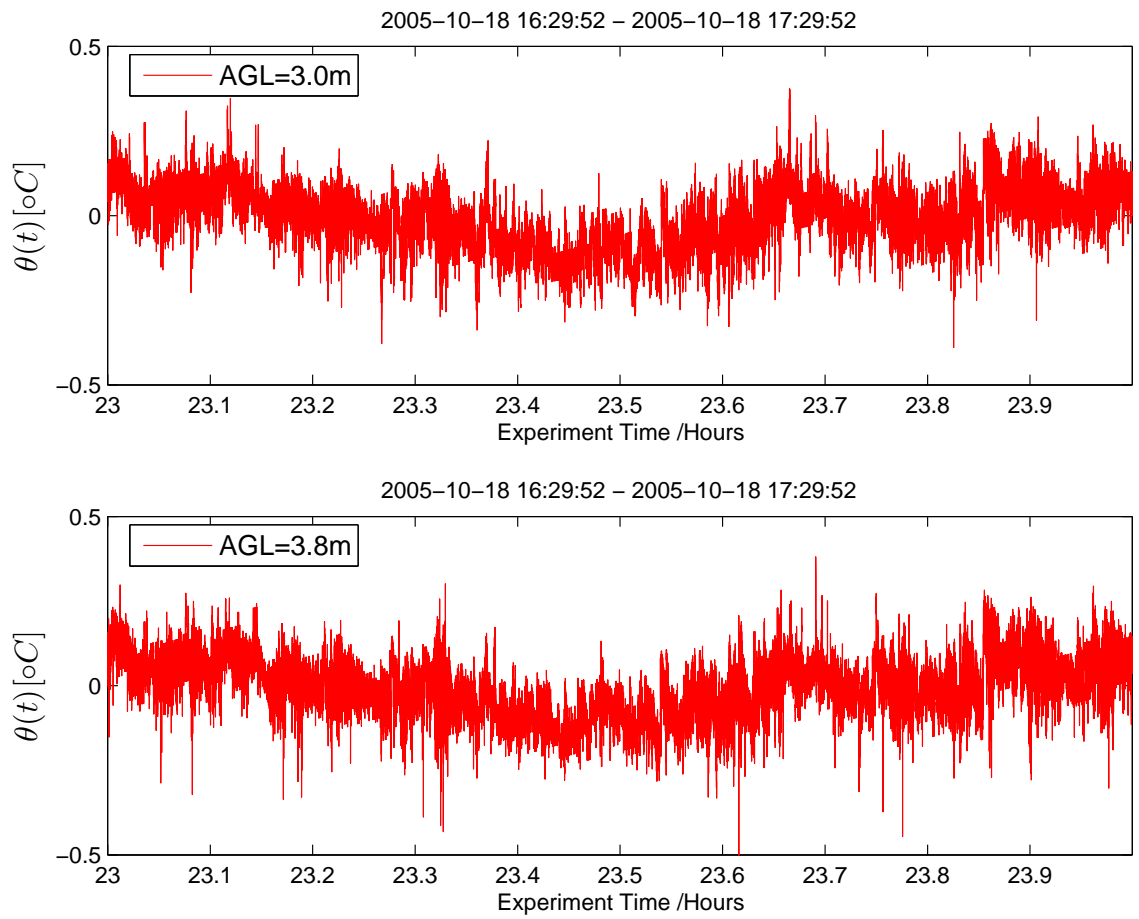


Figure 4.7. Time series of detrended temperature θ

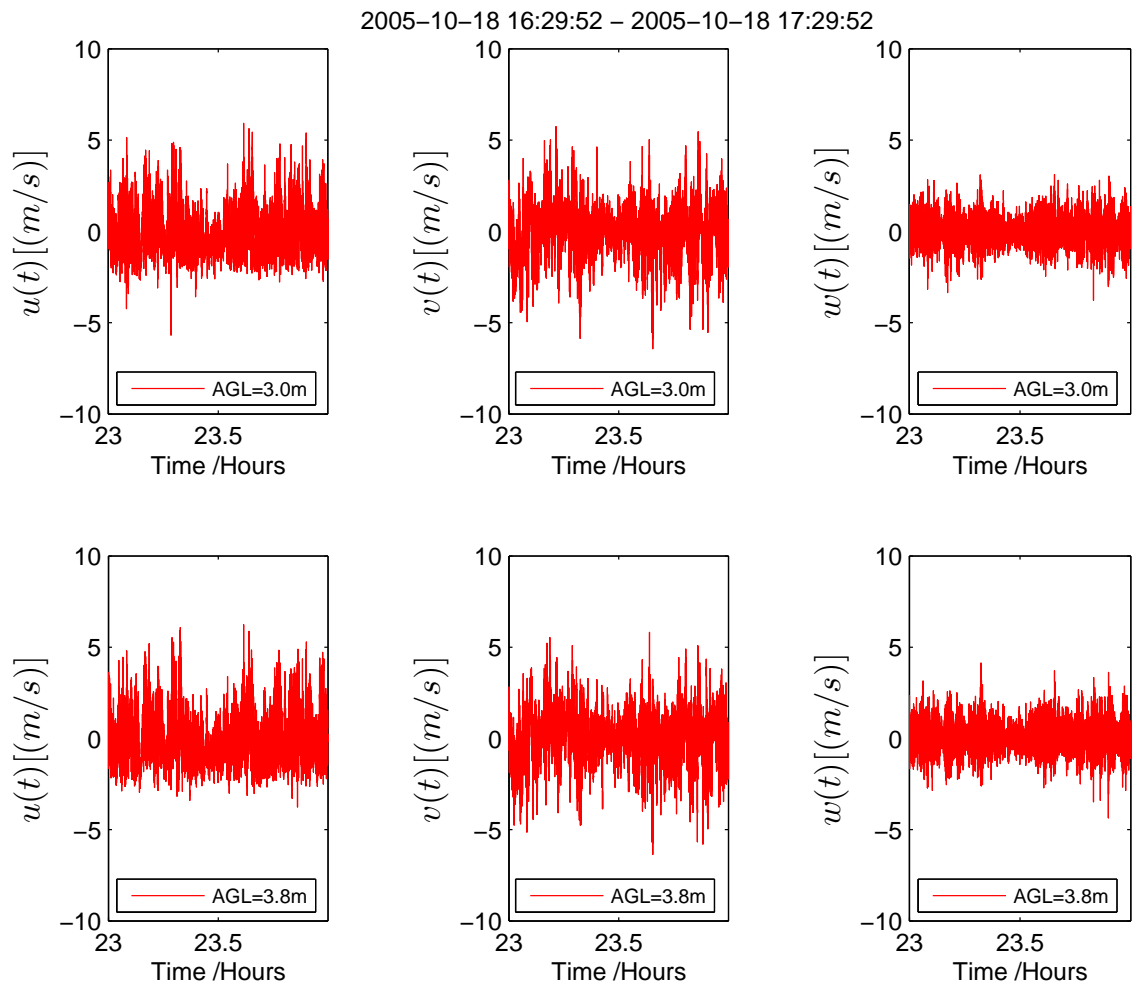


Figure 4.8. Time series of rotated and detrended wind velocity components u, v and w

$$\begin{aligned}
\sigma_{n\theta}^2 &\approx \Delta B_{m\theta}(\tau_s) \\
&= B_{m\theta}(0) - B_{m\theta}(\tau_s) \\
&= 0.0057K^2 - 0.0050K^2 \\
&= 0.0007K^2
\end{aligned} \tag{4.37}$$

or

$$\sigma_{n\theta} = 0.026K, \tag{4.38}$$

where $\sigma_{n\theta}^2$ is the variance of the noise added to the temperature time series, $\sigma_{n\theta}$ the corresponding standard deviation, $B_{m\theta}$ the measured ACF of the temperature plus noise and $\tau_s = 0.0314s$ the sampling interval, or first time lag. Trying to use equation [4.35] instead, with $U = 1.84\frac{m}{s}$, $C_\theta^2 = 0.02\frac{K^2}{m^3}$, $\tau_s = 0.0314s$ and $\Delta B_{m\theta}(\tau_s) = 0.0007K^2$, results in:

$$\begin{aligned}
\sigma_{n\theta}^2 &= \Delta B_{m\theta}(\tau_s) - \frac{1}{2}C_\theta^2 U^{2/3} \tau_s^{2/3} \\
&= 0.0007K^2 - \frac{1}{2}0.02\frac{K^2}{m^3}\left(1.84\frac{m}{s}0.0314s\right)^{\frac{2}{3}} \\
&= 0.0007K^2 - 0.00150K^2 = -0.0008K^2,
\end{aligned} \tag{4.39}$$

which cannot be true since there is no negative noise, and it is likely due to the explained spatial averaging effect.

4.5.2 Measurement Errors

To describe measurement performance the specification of sensors usually contains the terms *accuracy*, *precision*, *sensitivity* and/or *resolution*, which are reviewed in the following. The precision P (or sensitivity) is defined as the standard error of the fluctuation:

$$P = \sqrt{\langle(m' - t')^2\rangle}, \tag{4.40}$$

where m' are the measured fluctuations and t' are the true fluctuations. Now consider the standard error A (referred to as accuracy) of a non-zero-mean variable:

$$\begin{aligned}
 A &= \sqrt{\langle (m - t)^2 \rangle} \\
 &= \sqrt{\langle [(\langle m \rangle + m') - (\langle t \rangle + t')]^2 \rangle}
 \end{aligned}
 \tag{4.41}$$

The accuracies for the wind speed U and the temperature θ are given in table 4.3 and 4.4. In subsection 4.5.1 the noise in the temperature data was estimated as $\sigma_{n\theta} = 0.026K$. Assuming a normal distribution, 99.7% of all values are within $\pm 3\sigma_{n\theta} = \pm 0.078K$ of the mean value. This can be regarded as the precision of the temperature measurement, which is much better than the accuracy shown in table 4.4. It can be concluded that the mean value of the temperature is estimated much worse than the fluctuations of the temperature. To confirm the accuracy for temperature or velocity an external calibration standard would be needed.

For the wind speed U table 4.3 gives an equation to calculate the accuracy of the standard deviation σ_u . Choosing $\sigma_u = 1.1 \frac{m}{s}$ from the the dataset 2005-10-19 23:29:52 EDT to 2005-10-20 00:29:52 EDT gives:

$$\begin{aligned}
 A &= \pm \frac{1}{100} \sigma_u + \pm 0.05 \frac{m}{s} \\
 &= \pm \frac{1}{100} 1.1 \frac{m}{s} + \pm 0.05 \frac{m}{s} \\
 &= \pm 0.06 \frac{m}{s}
 \end{aligned}
 \tag{4.42}$$

While it was not possible to estimate the noise in the wind speed data in subsection 4.5.1, an order of magnitude estimate is possible from the power spectrum, as performed later in subsection 4.5.4. The standard deviation of the noise derived from the power spectrum is

$0.083 \frac{m}{s}$, which results in a precision of $\pm 0.24 \frac{m}{s}$. This of course is larger than $0.06 \frac{m}{s}$. As pointed out in subsection 4.5.4 as well, this value is overestimated and nevertheless agrees by a factor of about four to five with the range of the accuracy. A typical sensor contains an

Range	0 to 40 m/s
Resolution	0.01 m/s
Threshold	0.01 m/s
Accuracy	$\pm 1 \% \text{ rms } \pm 0.05 \text{ m/s (0 to 30 m/s)}$ $\pm 3 \% \text{ rms (30 - 40 m/s)}$

Table 4.3. Performance on wind speed from R.M. Young Company (1999)

Range	$-50^{\circ}C \text{ to } 50^{\circ}C$
Resolution	$0.01^{\circ}C$
Accuracy	$\pm 2^{\circ}C \text{ (0 to 30 m/s)}$

Table 4.4. Performance on temperature from R.M. Young Company (1999)

analog to digital converter (ADC) with a certain number of bits N_{ADC} . Then the resolution R or the quantization step Q (assuming linear quantization) is defined as:

$$R = Q = \frac{range}{2^N} \quad (4.43)$$

where *range* is the allowed input range of the sampled analog signal, which can be uni- or bipolar. Thus the value of the resolution is not useful for any performance description. However, it should be better than the precision and the accuracy, otherwise it will limit the performance. It can be seen from table 4.3 and 4.4 that these requirements are fulfilled for the used sonic.

4.5.3 Autocovariance Function and Structure Function

In figure 4.9 the ACF of the velocity component u is shown for the measurement heights of 3.0 m and 3.8 m. The maximum lag used is $\tau = 600s$. It can be seen that there are two distinct time lag ranges. The first is around the zero lag up to about $|\tau| \approx 50 - 60s$, and the other one is the range beyond this.

Following Orlanski (1975), the time and length scales of atmospheric processes can be divided in categories of micro-, meso- and macro-scales. These categories can further be subdivided into subcategories named gamma, beta and alpha. From figure 4.10, it can be seen that the range in the vicinity of the zero lag is denoted the micro-gamma region with time-scales until 1 min and length-scales until 20 m. An extract of atmospheric processes classified by Orlanski (1975) for the micro range is shown in table 4.5.

To extract the turbulent structure parameter C_f^2 , the structure function $D_f(\tau)$ is computed assuming stationarity from the ACF $B_f(\tau)$ using equation [2.18]. Figure 4.11 shows $D_u(\tau)$ computed from $B_u(\tau)$ shown in figure 4.9. Ideally the structure function approaches, for large time lags τ , a constant value of $2B_f(\tau) = 2\sigma_f^2$. In 4.11, the asymptotic behavior is approximately reached at about $\tau = 1\text{min}$.

Range	Time Scale τ	Length Scale R	Processes
Micro-Gamma	$\tau \leq 1 \text{ min}$	$R \leq 20\text{m}$	Plumes Roughness Turbulence
Micro-Beta	$1\text{min} \leq \tau \leq 5 \text{ min}$	$20\text{m} \leq R \leq 200\text{m}$	Dust Devils Thermals Wakes
Micro-Alpha	$5\text{min} \leq \tau \leq 30 \text{ min}$	$200\text{m} \leq R \leq 2000\text{m}$	Tornadoes Deep Convection Short Gravity Waves

Table 4.5. Atmospheric processes in the micro scale after Orlanski (1975)

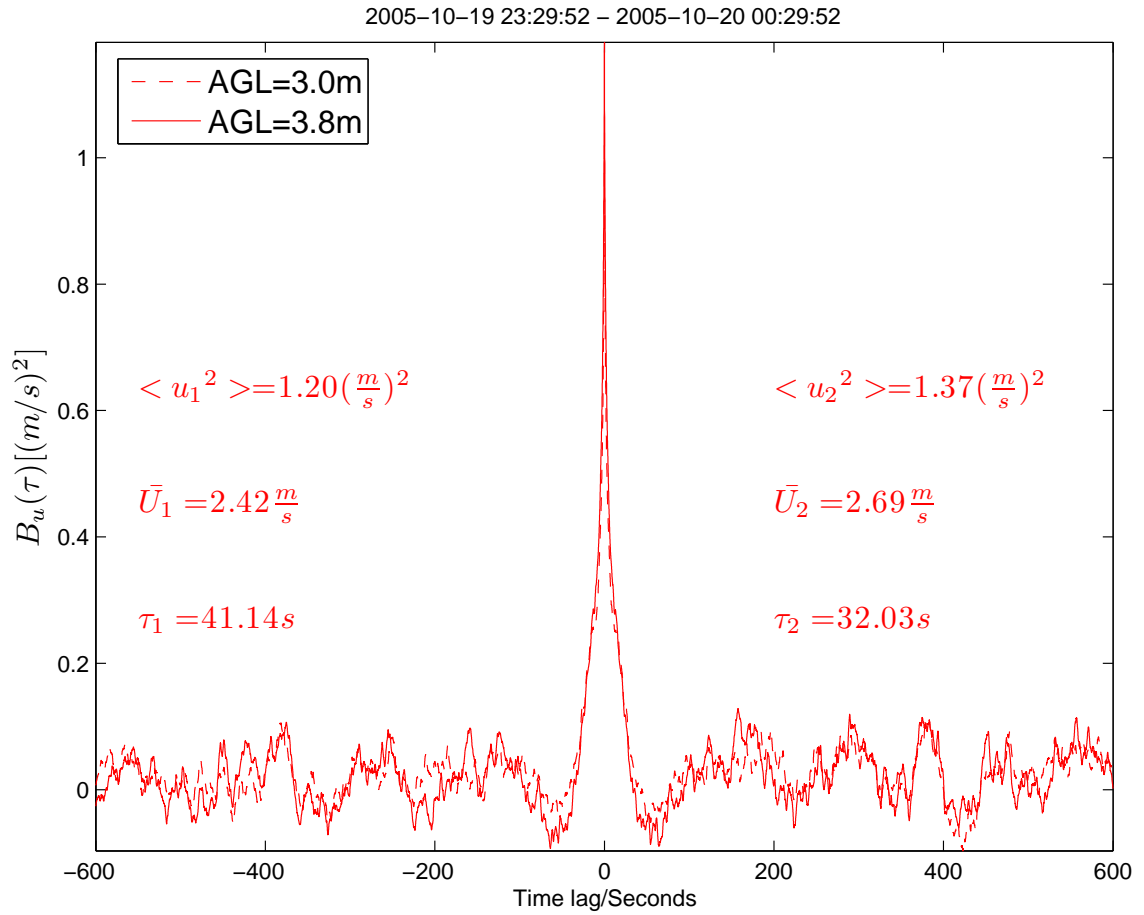


Figure 4.9. ACF of u with a maximum time lag $\tau = 600s$ for sonic 1 and 2

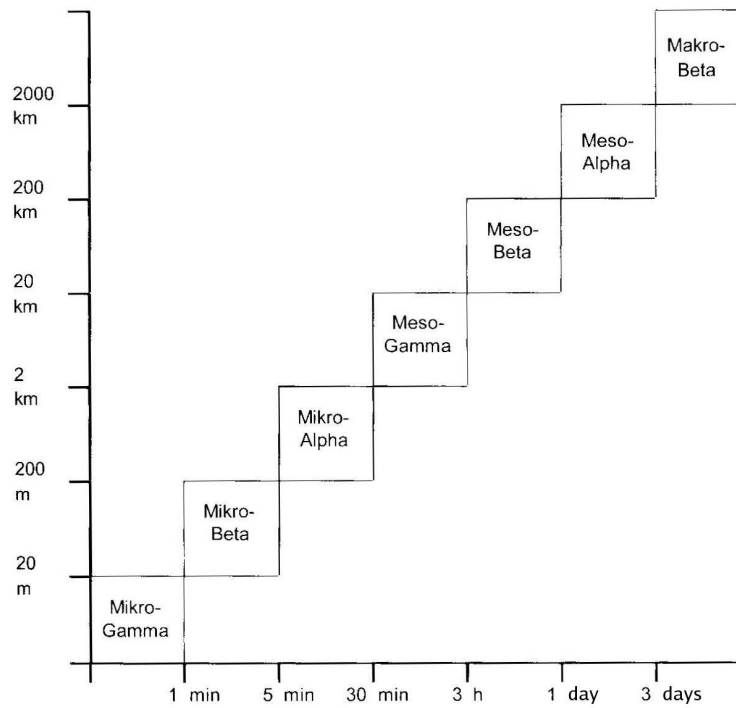


Figure 4.10. Scales of atmospheric processes; after Orlandi (1975); diagram from Foken (2003)[p.5]

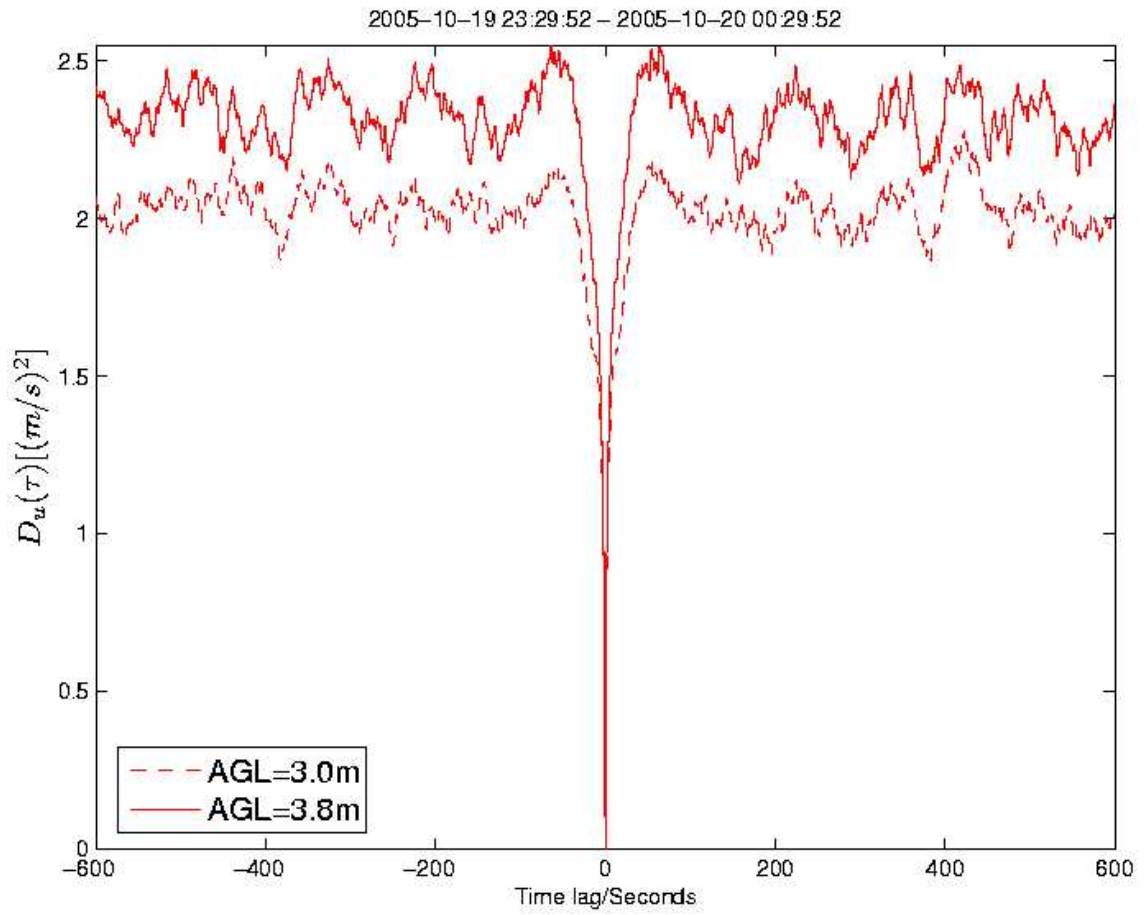


Figure 4.11. Structure function of u with a maximum time lag $\tau = 600s$ for sonic 1 and 2

4.5.4 Periodogram and Power spectrum

While subsection 4.5.3 described turbulence from a time-domain perspective, a spectral description in the form of the power spectrum or the wavenumber spectrum is often more useful. Several ways are available to estimate the one-sided power spectrum $S_f(\omega)$, one of which is to use the Wiener-Khintchine relationship [2.21] and equation [2.43] based on the Fourier transformation of the ACF:

$$S_f(\omega) = 2W_f(\omega) = 2\frac{1}{2\pi} \int_{-\infty}^{\infty} e^{-j\omega\tau} B_f(\tau) d\tau. \quad (4.44)$$

Another method is the direct Fourier transformation (FT) of the time series to obtain the spectrum $L_f(\omega)$ as the properly normalized magnitude square of the FT:

$$S_f(\omega) = 2W_f(\omega) = 2L_f(\omega)L_f(\omega)^* = 2|L_f(\omega)|^2. \quad (4.45)$$

Note that the spectrum computed by this method cannot have any imaginary part, because of the absolute operation involved.

The one-sided power spectrum $S_f(\omega)$ is also known as the variance spectrum, because of the following property:

$$\sigma_f^2 = \int_0^{\infty} S_f(\omega) d\omega, \quad (4.46)$$

which is the requirement for a computed one-sided power spectrum to be correctly normalized. Table 4.6 shows such a computation done for the power spectra of u, v, w and θ computed from the dataset using both described spectral methods and directly from the time series. The values shown agree well with each other, as expected. The power spectrum $S_f(\omega)$ of a random time function should strictly be distinguished from the *raw power spectrum* or the *periodogram*, denoted $\hat{S}_f(\omega)$. The latter one is a random function of ω , while the power spectrum is a deterministic function of ω .

However the periodogram can be smoothed to give an estimate of the power spectrum. The

Variable	Time series	FFT direct	FFT ACF
σ_u^2 $[(\frac{m}{s})^2]$	1.1971	1.1971	1.1970
σ_v^2 $[(\frac{m}{s})^2]$	0.7611	0.7611	0.7610
σ_w^2 $[(\frac{m}{s})^2]$	0.3169	0.3169	0.3168
σ_θ^2 $[K^2]$	0.0407	0.0407	0.0407

Table 4.6. Variance computed from time series, direct FFT and ACF FFT

spectral smoothing technique applied is logarithmic-equidistant-averaging, which averages all data values in a logarithmic constant intervals of a given width, as used in Siebert and Muschinski (2001). Figure 4.12 shows an example of the real and imaginary parts of the periodogram and the power spectrum of u computed using the ACF. Note that the imaginary part is nearly flat over the spectrum and about 10 orders of magnitudes smaller than the real part, which designates it as numerical noise due to unavoidable rounding errors. There should indeed be no imaginary part due to the computation, since the ACF is an even and real function, and the Fourier transformation of an even and real function is purely real. Thus the results of the real operation and the absolute operation become identical. The periodogram and the power spectrum are shown in figure 4.13 for the method using the ACF to compute the FFT and in figure 4.14 for the method using the time series directly. Now comparing figure 4.13 and figure 4.14 the power spectrum with the $f^{-\frac{5}{3}}$ law shows a good agreement for nearly two decades from about 0.2 Hz to 10 Hz. However at frequencies between 10 Hz and the Nyquist frequency of 16 Hz a slight flattening of the spectrum can be seen. Reasons for this can be that the noise level of the sonic is reached or that energy is aliasing back from above the Nyquist frequency.

It is possible to conservatively estimate the variance of the noise as following:

$$\sigma_n^2 = \int_0^{\omega_{nyq}} S_n(\omega) d\omega = S_n \int_0^{\omega_{nyq}} d\omega, \quad (4.47)$$

where ω_{nyq} is the angular Nyquist frequency. Assuming a flat noise floor and that the smoothed measured power spectrum is severely limited by noise at the Nyquist frequency

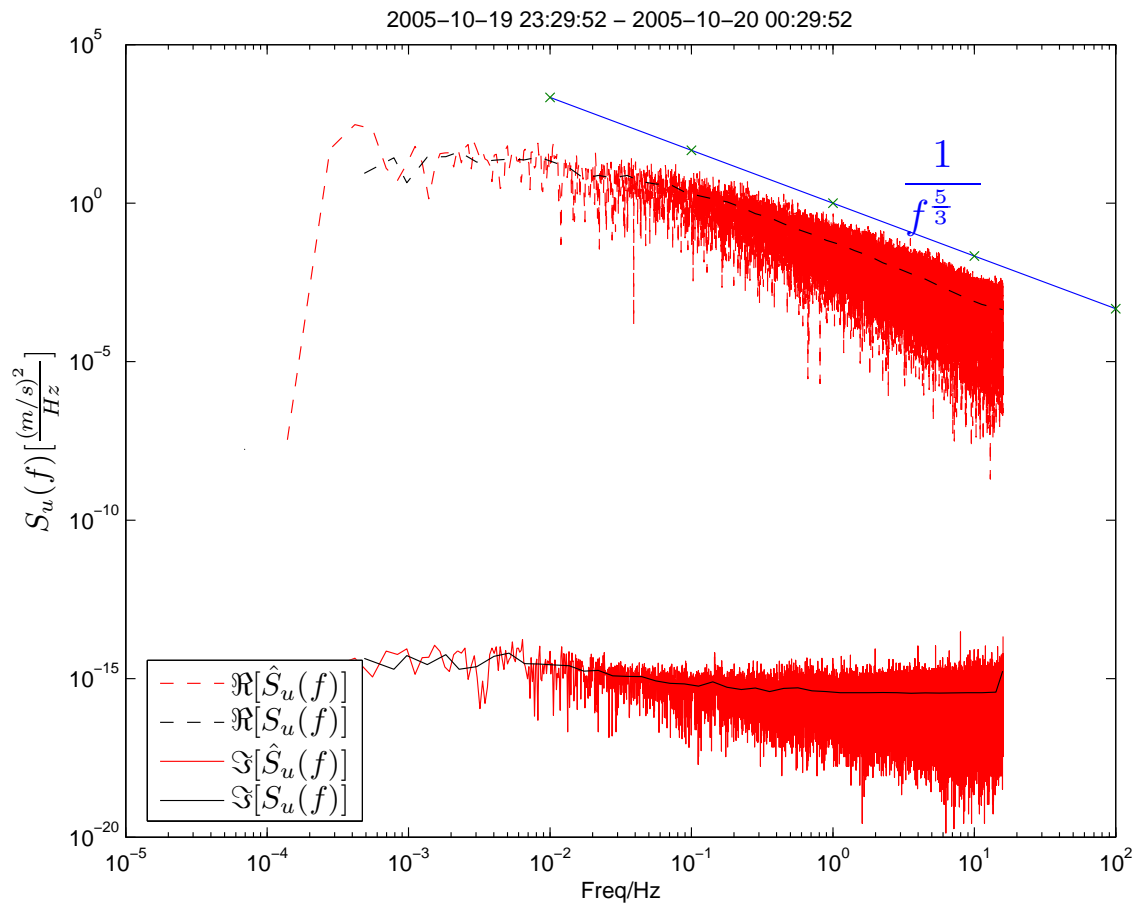


Figure 4.12. Real and imaginary parts of periodogram and power spectrum of u time series computed from ACF

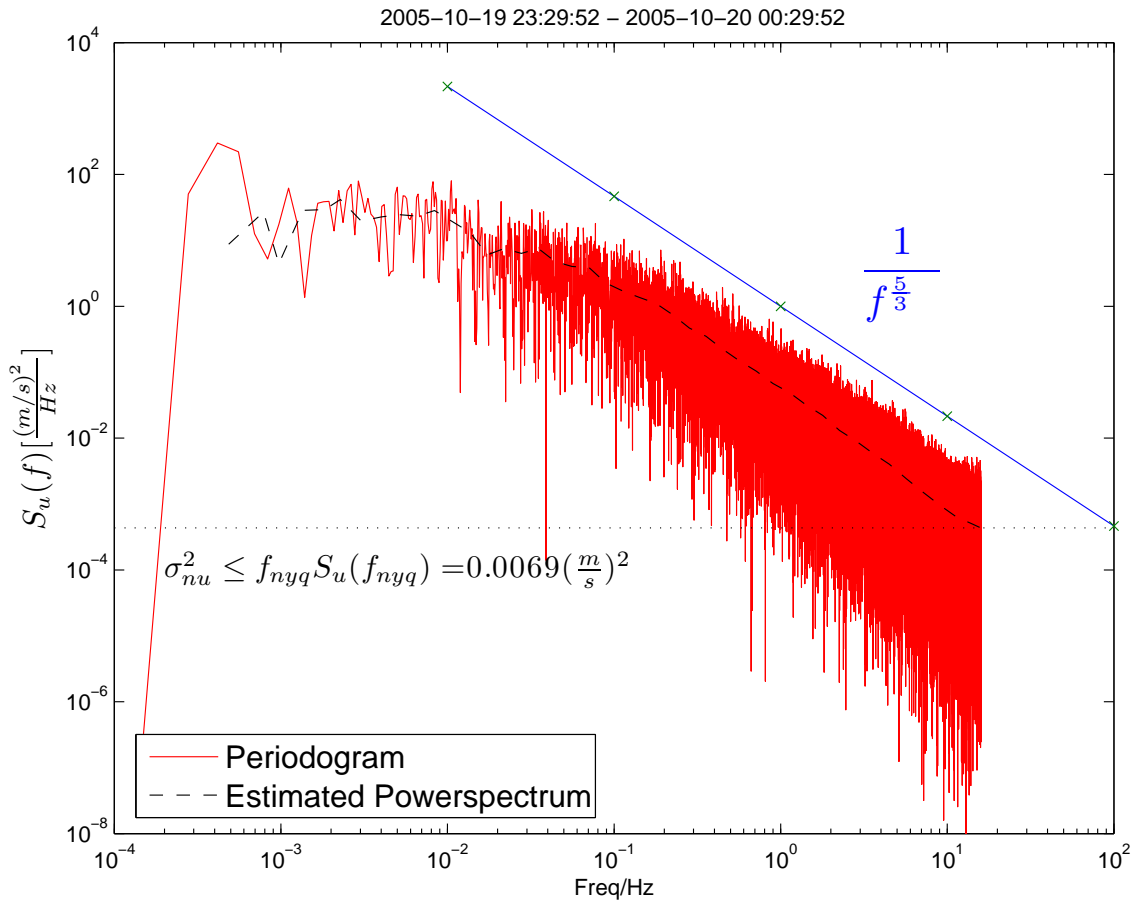


Figure 4.13. Periodogram and power spectrum of u time series computed from ACF

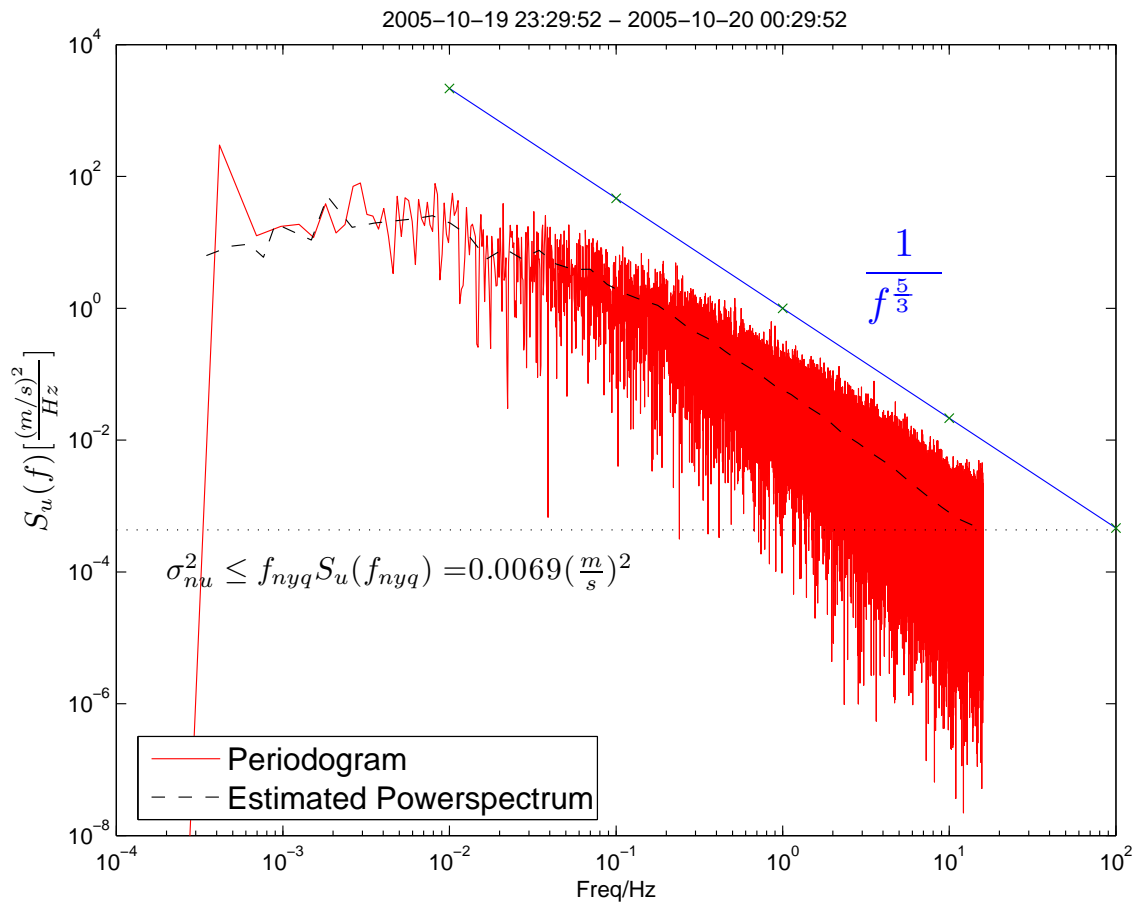


Figure 4.14. Periodogram and power spectrum of u time series computed directly from time series

equation [4.47] can be written as:

$$\sigma_n^2 = S_f(\omega_{nyq})\omega_{nyq}. \quad (4.48)$$

Table 4.7 lists the variance of the noise for all velocity components and for temperature

Variable	FFT direct	FFT ACF	ACF
σ_{nu}^2 [$(\frac{m}{s})^2$]	0.0069	0.0069	N/A
σ_{nv}^2 [$(\frac{m}{s})^2$]	0.0088	0.0088	N/A
σ_{nw}^2 [$(\frac{m}{s})^2$]	0.0102	0.0103	N/A
$\sigma_{n\theta}^2$ [K^2]	0.00069	0.00069	0.0007

Table 4.7. Variance of noise computed from power spectrum and ACF

Variable	FFT direct	FFT ACF	ACF	Siebert and Muschinski (2001)
σ_{nu} [$\frac{m}{s}$]	0.083	0.083	N/A	0.02
σ_{nv} [$\frac{m}{s}$]	0.093	0.093	N/A	0.02
σ_{nw} [$\frac{m}{s}$]	0.101	0.101	N/A	0.02
$\sigma_{n\theta}$ [K]	0.026	0.026	0.026	0.02

Table 4.8. Standard deviation of noise computed from power spectrum and ACF

using the spectral techniques. Table 4.8 shows the corresponding standard deviations and, in addition, values measured by Siebert and Muschinski (2001) with a similar sonic. It can be seen that the variance of the noise in the temperature data agrees well with all three methods, and is close to the value from Siebert and Muschinski (2001). The variance of the noise in the velocity components might have been overestimated because the flattening in the power spectra is not very strong and there is no visual noise spike in the ACF of the velocity components. Comparing the velocity components to the smaller values retrieved by Siebert and Muschinski (2001) supports this interpretation.

In figure 4.15 the power spectra of the velocity components are computed with the two described spectral methods and plotted. It can be seen that both spectral analysis methods

lead to very similar results. Further, it can be noted that all obey the $5/3$ law over a range of nearly two decades. However $S_w(f)$ has a significant lower power density at lower frequencies, which can be explained by the presence of the ground. The ground prevents large-scale or long-term vertical motion at low heights (assuming the ground is horizontal and flat). Similarly in figure 4.16 the temperature power spectrum is plotted for both spec-

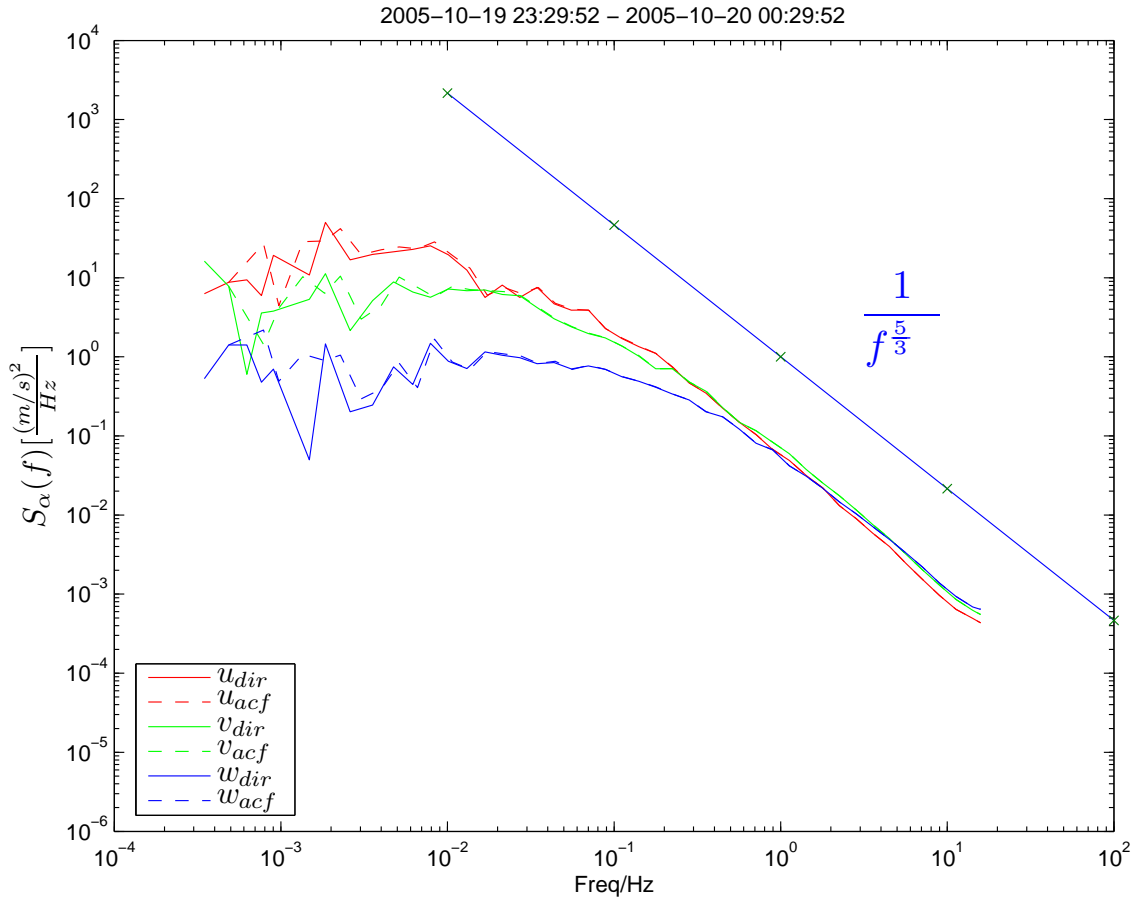


Figure 4.15. Power spectrum of velocity component time series computed directly and from ACF

tral methods, which again show agreement and follow the $5/3$ law. The effect of the noise floor, however, is much more visible, compared to the velocity power spectra. This is indicated by a stronger flattening of the power spectrum near the nyquist frequency, caused by

the lower signal-to-noise ratio (SNR) of the temperature measurements compared to that of the velocity.

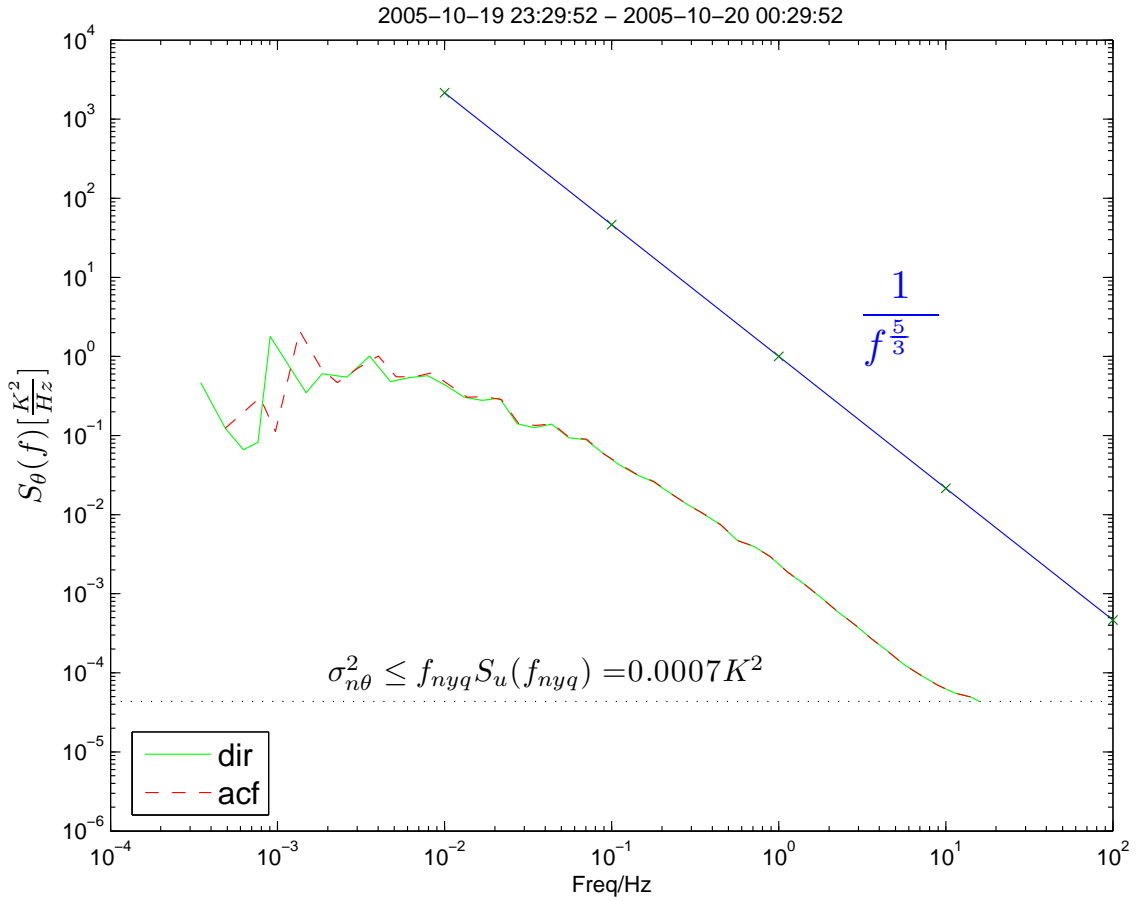


Figure 4.16. Power spectrum of temperature time series computed directly and from ACF

4.5.5 Inertial Subrange and Structure Parameter

In subsection 4.5.3 the structure function $D_f(\tau)$ was computed and an example for $D_u(\tau)$ was given in figure 4.11. The turbulent structure parameter C_f^2 can be computed from $D_{f=u}(\tau)$ based on equation [2.40]:

$$C_f^2(\tau) = \frac{D_f(\tau)}{U^{2/3}\tau^{2/3}}. \quad (4.49)$$

In figure 4.17 the velocity structure parameters $C_u^2(\tau)$, $C_v^2(\tau)$ and $C_w^2(\tau)$ are shown while in figure 4.18 the temperature structure parameter $C_\theta^2(\tau)$ is plotted. It needs to be kept in mind that equation [4.49] is valid only for the inertial subrange. This range can be recognized as a plateau. In addition, the $2B_f(0)$ asymptote is plotted. The intersection of the 2/3 law and the $2B_f(0)$ asymptote can be defined as the intersection time lag τ_0 (here τ_u, τ_v, τ_w and τ_θ respectively). Values of the structure parameters can also be derived from the power

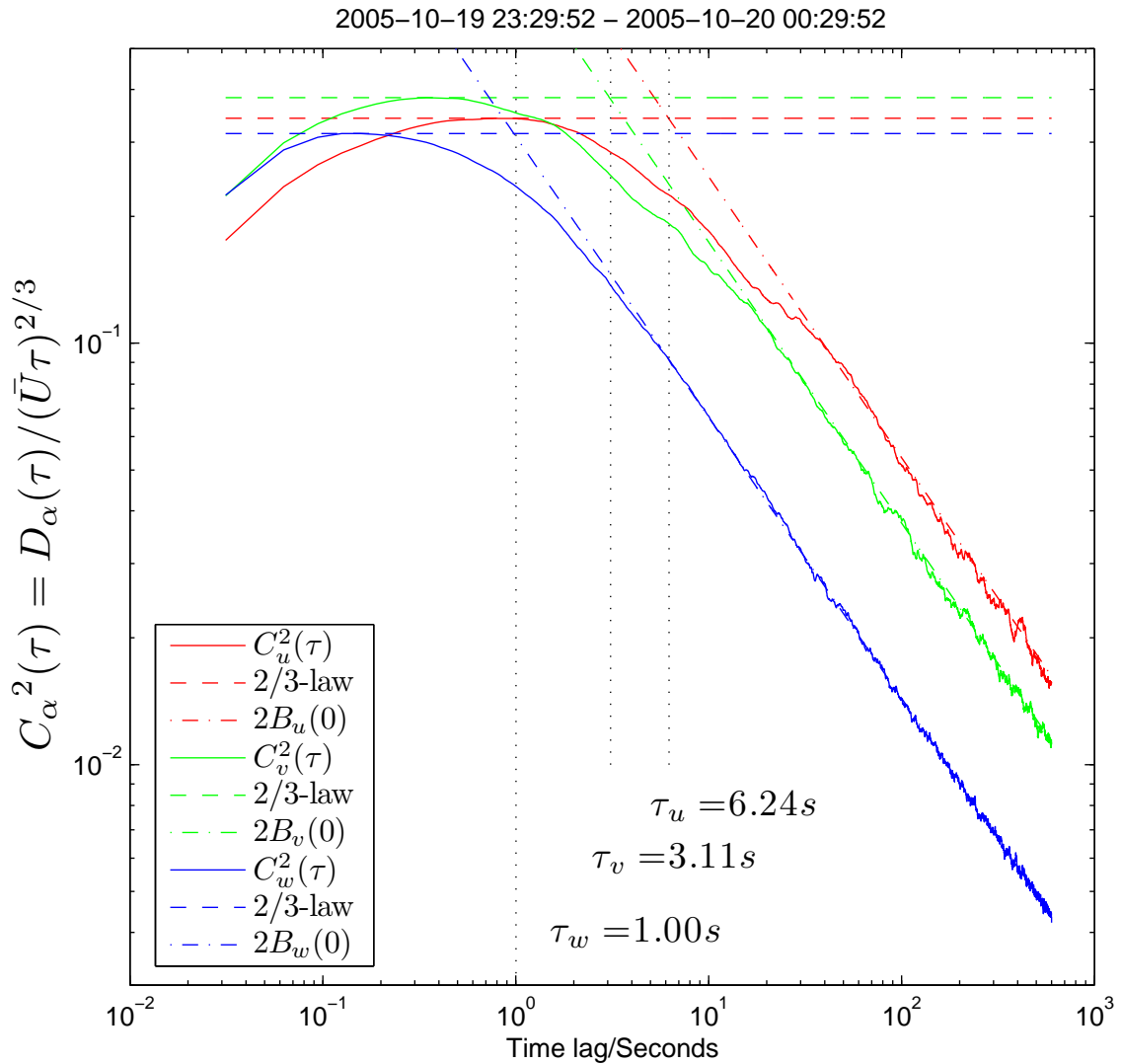


Figure 4.17. Structure parameter of velocity components from structure functions

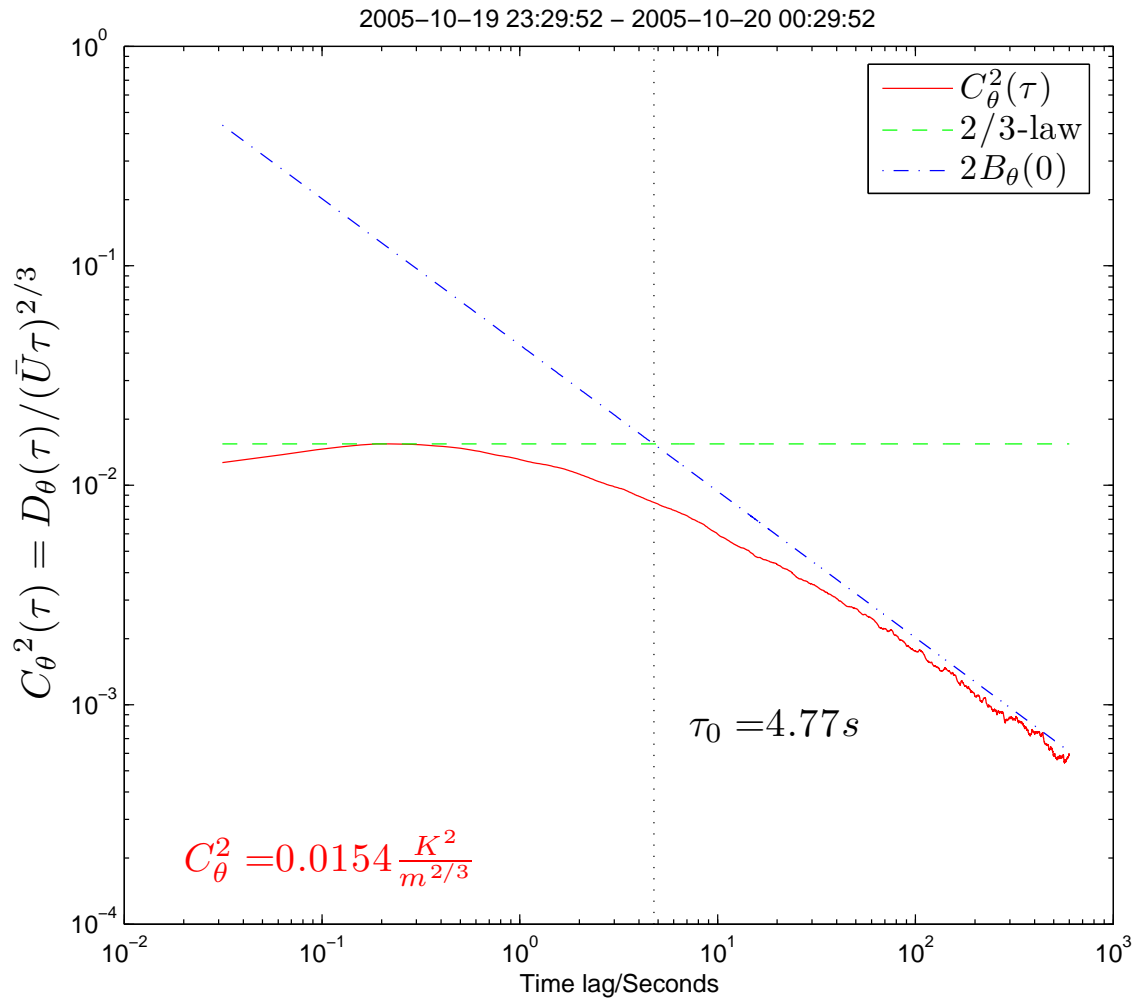


Figure 4.18. Structure parameter of temperature $C_{\theta}^2(\tau)$ from structure function

spectra by rewriting equation [2.45] as:

$$C_f^2(f) = 4.02 S_f(f) \left[\frac{2\pi}{U} \right]^{\frac{2}{3}} f^{\frac{5}{3}}. \quad (4.50)$$

Figure 4.19 shows the results from equation [4.50] for the velocity structure parameter and figure 4.20 shows the structure parameter of the temperature derived from the power spectrum.

Table 4.9 lists the structure parameter derived with the spectral methods and the structure function. It can be seen that in all cases C_v^2 is the largest, followed by C_u^2 and then C_w^2 . While both spectral methods agree closely between themselves, the values extracted from the structure function deviate from them. In the case of deriving the structure parameter from the structure function only a peak instead of a well defined plateau is indicating the 2/3 law, and therefore the inertial subrange. Therefore structure parameter can only be chosen as the maximum. However, this is not the case when it is derived from the spectral methods, in which case the inertial subrange is wider and can be recognized as a plateau in figure 4.19 and 4.20 at higher frequencies.

Comparing these two ways (spectral methods and structure function), the way using the spectral methods provides a much wider inertial subrange, which allows for a better estimate of the structure parameter, rather than just using the peak value from the structure function estimate.

Variable	FFT direct	FFT ACF	Structure Function
C_u^2 $\left[\left(\frac{m/s}{m^{2/3}} \right)^2 \right]$	0.4529	0.4532	0.3415
C_v^2 $\left[\left(\frac{m/s}{m^{2/3}} \right)^2 \right]$	0.5506	0.5512	0.3823
C_w^2 $\left[\left(\frac{m/s}{m^{2/3}} \right)^2 \right]$	0.3868	0.3869	0.3145
C_θ^2 $\left[\frac{K^2}{m^{2/3}} \right]$	0.0173	0.0173	0.0154

Table 4.9. C_α^2 computed from power spectra and structure function

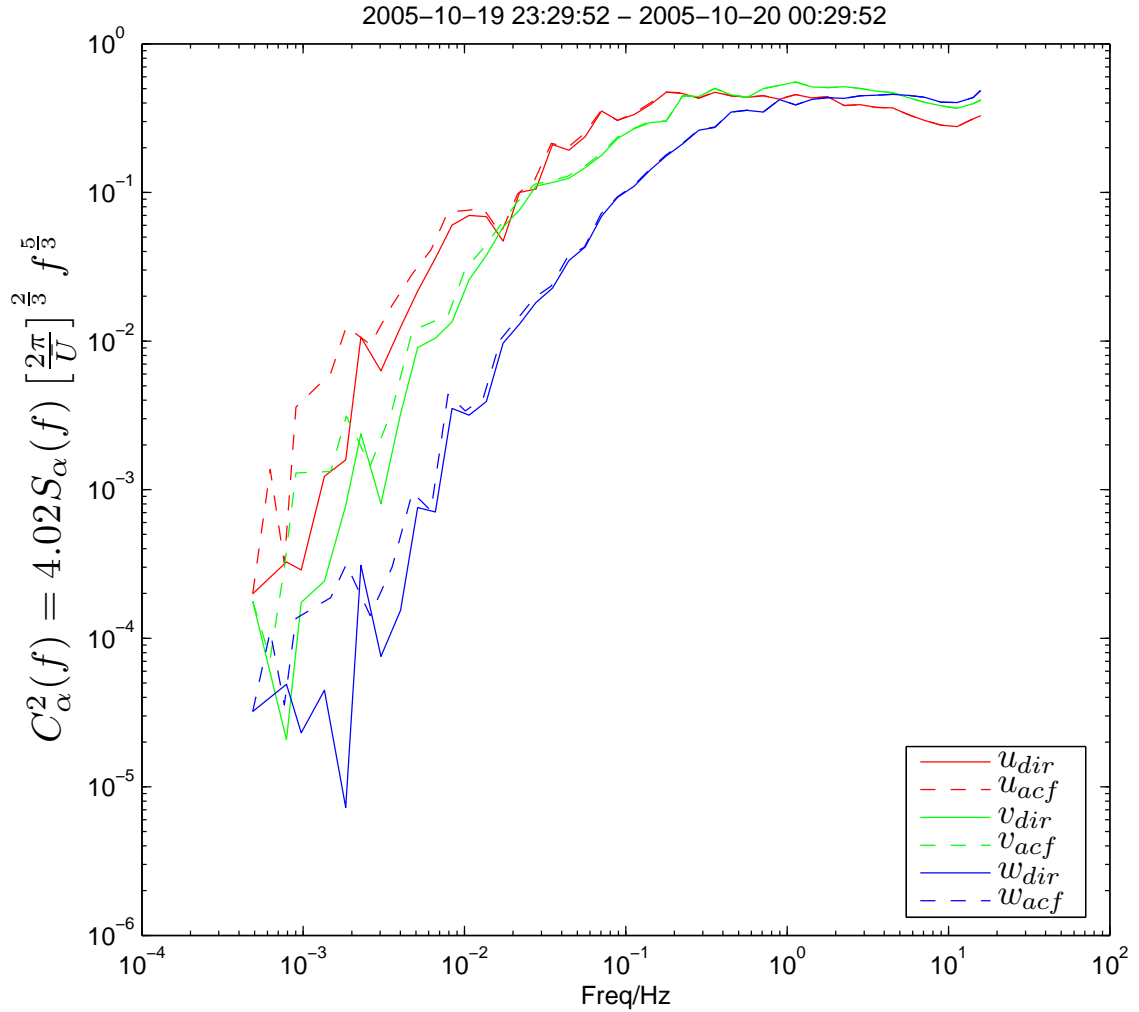


Figure 4.19. Structure parameter of velocity components from power spectrum

4.5.6 Integral Time and Length Scales

The intersection time lag τ_0 given in subsection 4.5.5 can be determined from the ACF by assuming a 2/3 dependence in following form:

$$B_f(\tau) = B_f(0) - \frac{1}{2}D_f = \sigma_f^2 - \frac{1}{2}C_f^2\bar{U}^{2/3}|\tau|^{2/3}, \quad (4.51)$$

where equation [2.40] was inserted into equation [2.18] to resolve equation [4.51]. To find the intersection point of the $2B_f(0)$ -asymptote and the 2/3 law, equation [4.51] can be

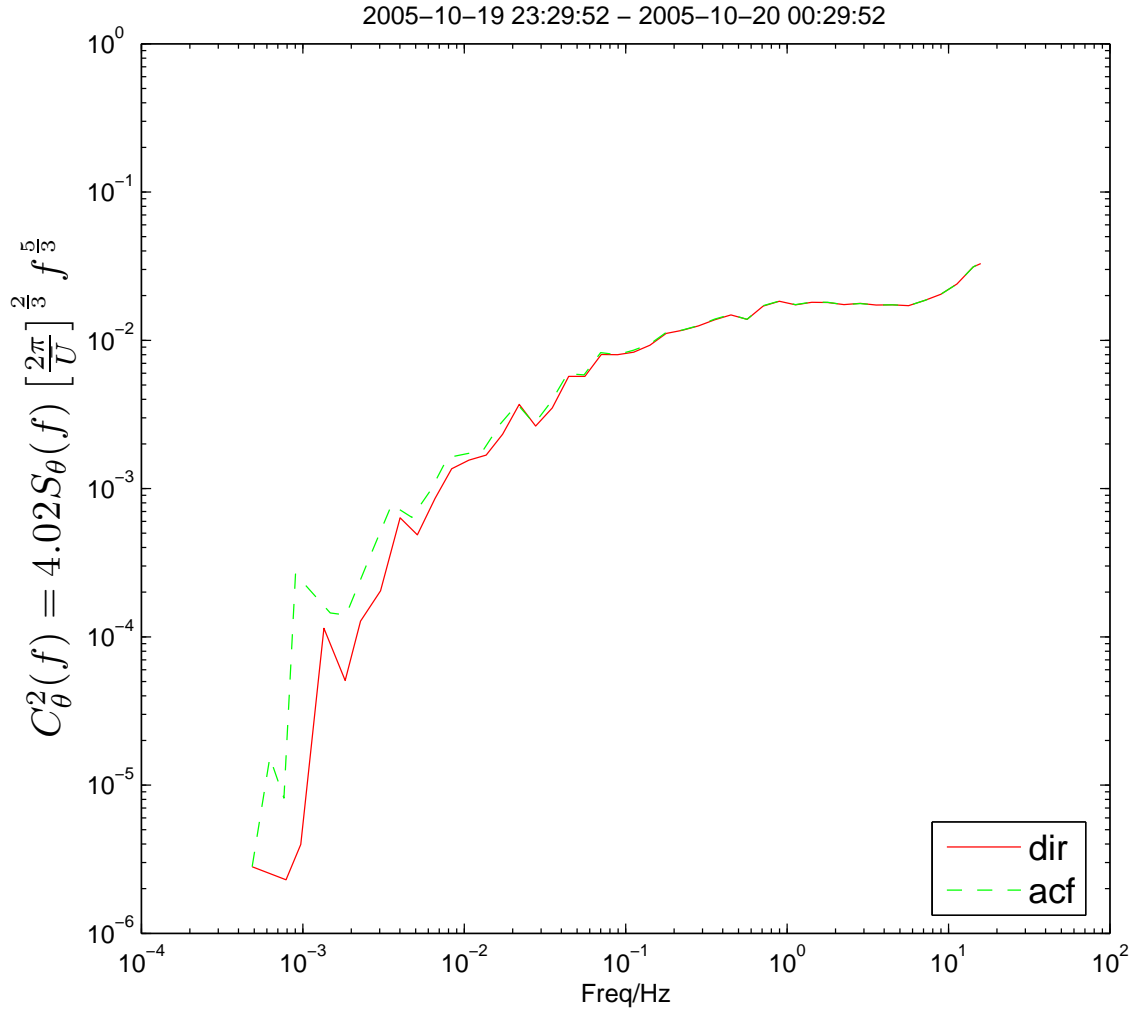


Figure 4.20. Structure parameter of temperature from power spectrum

rewritten as:

$$2\sigma_f^2 = C_f^2 \bar{U}^{\frac{2}{3}} \tau_0^{\frac{2}{3}}, \quad (4.52)$$

where the time lag τ was set to the intersecting time lag τ_0 . The intersection time lag τ_0 can now be written as:

$$\tau_0 = 2^{\frac{3}{2}} \frac{\sigma_f^3}{[C_f^2]^{\frac{3}{2}} \bar{U}}. \quad (4.53)$$

Using equation [2.31], insert [4.51] and assuming $B_f(\tau) = 0$ for $\tau \geq \tau_i$, τ_i can be written as:

$$\begin{aligned}
\tau_i &= \frac{1}{B_f(0)} \int_0^{\tau_i} B_f(\tau) d\tau \\
&= \frac{2}{B_f(0)} \int_0^{\tau_i} \sigma_f^2 - 0.5C_f^2\bar{U}^{2/3}|\tau|^{2/3} d\tau \\
&= 2\tau_0 - \frac{C_f^2\bar{U}^{2/3}}{\sigma_f^2} \frac{3}{5}\tau_0^{\frac{5}{3}} \\
&= 2 \left[2^{\frac{3}{2}} \frac{\sigma_f^3}{[C_f^2]^{\frac{3}{2}}\bar{U}} \right] - \frac{C_f^2\bar{U}^{2/3}}{\sigma_f^2} \frac{3}{5} \left[2^{\frac{3}{2}} \frac{\sigma_f^3}{[C_f^2]^{\frac{3}{2}}\bar{U}} \right]^{\frac{5}{3}} \\
&= \left[2^{\frac{5}{2}} - \frac{3}{5}2^{\frac{5}{2}} \right] \frac{\sigma_f^3}{[C_f^2]^{\frac{3}{2}}\bar{U}} \\
&= \frac{4}{5}\tau_0.
\end{aligned} \tag{4.54}$$

Figures 4.21, 4.22, 4.23 and 4.24 show the application of this technique, from here it can be seen that the analytical result for the relationship $\tau_i = \frac{4}{5}\tau_0$ from equation [4.54] is confirmed by the numerical integration over $B_{fit}(\tau)$. Using Taylor's hypothesis the integral time scale τ_i can be converted into the integral length scale r_i :

$$r_i = \bar{U}\tau_i \tag{4.55}$$

and correspondingly for the integral scales of the angular frequency ω_i (spectral width) and the wavenumber κ_i :

$$\omega_i = \bar{U}\kappa_i. \tag{4.56}$$

Table 4.10 shows the results of the integral scales calculated using equations [4.55], [4.56], [2.33] and [2.36]. Two effects on the length scales can be seen in table 4.10. First the length scale $r_{iw} = 1.93$ m of w is much smaller than the length scale $r_{iu} = 12.10$ m of u and the length scale $r_{iv} = 6.00$ m of v . Secondly the length scale of w is about 1/3 less than the height $z = 3$ m, while the length scales of u and v are twice and four times the height z respectively. Looking at ACF's shown in figure 4.23 for w , in figure 4.21 for u and 4.22 for v , a faster decline of the ACF for w can be seen then for u and v . Another observation

Var.	Time Scale τ_i [s]	Length Scale r_i [m]	Spectral Width ω_i [$\frac{1}{s}$]	Spectral Width f_i [Hz]	Spectral Width κ_i [$\frac{1}{m}$]
u	4.99	12.10	1.26	0.20	0.52
v	2.48	6.00	2.53	0.40	1.05
w	0.80	1.93	7.76	1.23	3.26
θ	3.81	9.24	1.64	0.26	0.68

Table 4.10. Integral scales

is that u has the largest length scale. This is consistent with the idea that the ground limits the length scale of w as mentioned before.

Another way to analyze the length scale and the time scale is to compute their values for 1-hour blocks over the whole experiment time and to compare their behavior to the mean wind speed computed over the same time interval. Figure 4.25 shows the mean wind speed U and the integral time scale τ_{iu} . Using equation [2.39] the integral length scale r_{iu} as a function of time is plotted in figure 4.26. Calculating the mean value \bar{r}_{iu} and the median value $median(r_{iu})$ of the integral length scale r_{iu} shown in figure 4.26 results in:

$$\bar{r}_{iu} = 12.05\text{m} \quad (4.57)$$

and

$$median(r_{iu}) = 10.67\text{m}. \quad (4.58)$$

It can be observed that U and τ_{iu} are inversely correlated to each other in figure 4.25, while in figure 4.26 it can be seen that the integral length scale has a much more constant behavior. From this, it can be said that the size of the stream wise mean velocity length scale does not depend much on the wind speed. Instead it can be found in Muschinski and Roth (1993) and Muschinski et al. (2004) that it depends on the height z and it is known as the largest measurable wavelength or the *isotropic cut-off wavelength* λ_{iu} . It was found to be:

$$\lambda_{iu} = 4z. \quad (4.59)$$

Using a height $z=3\text{m}$ results in a wavelength of 12m , which is a close match to the mean value and of the same order as the median value computed before. Notice, that strictly speaking the integral length scale r_{iu} and the isotropic cut-off wavelength λ_{iu} are not necessarily identical, but they should be of the same order of magnitude.

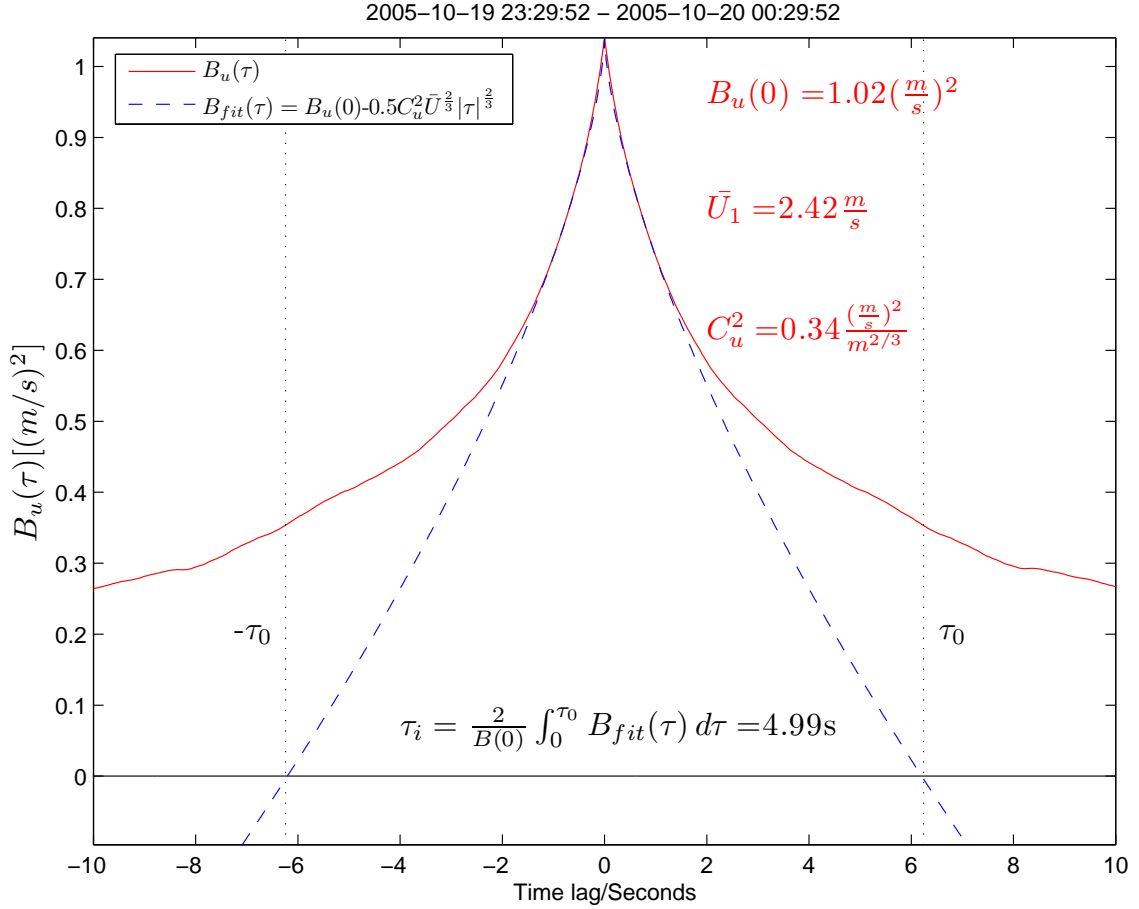


Figure 4.21. Autocovariance function $B_u(\tau)$ and integral time scale τ_{iu}

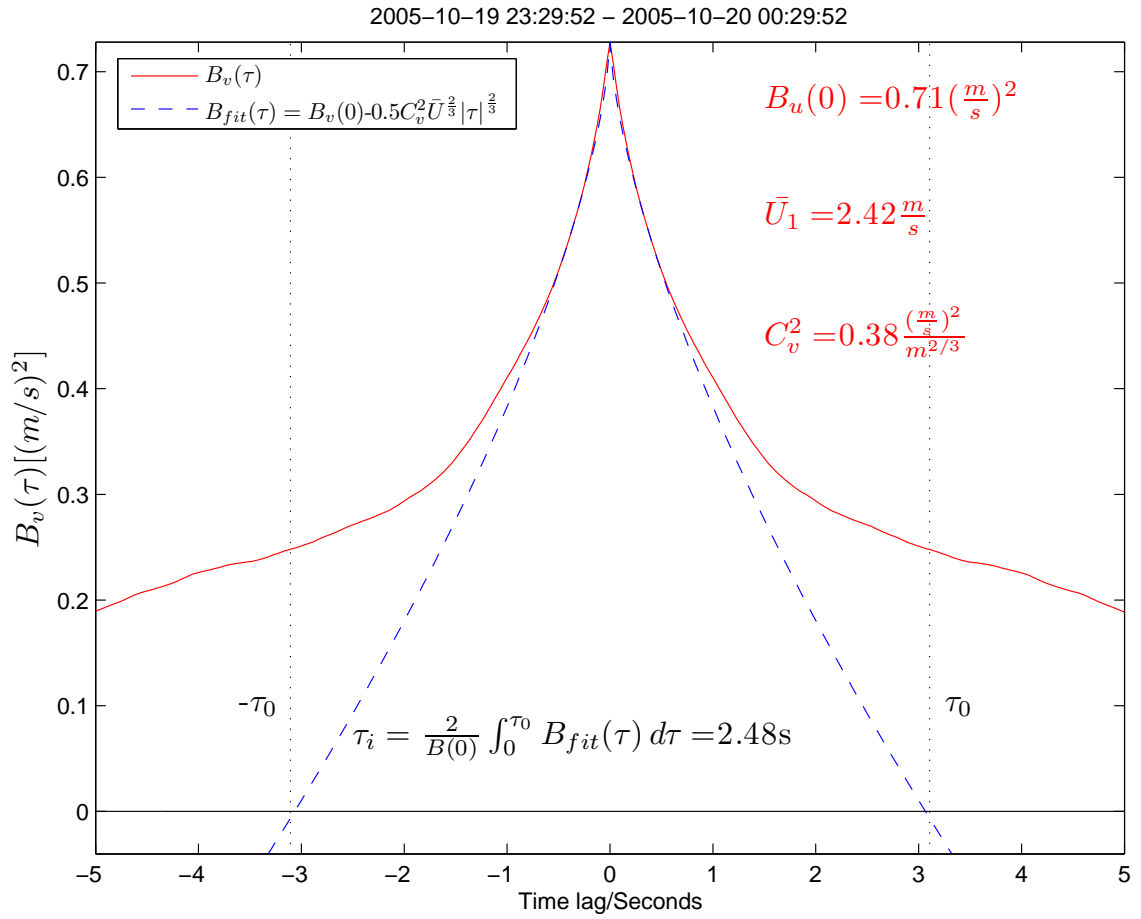


Figure 4.22. Autocovariance function $B_v(\tau)$ and integral time scale τ_{iv}

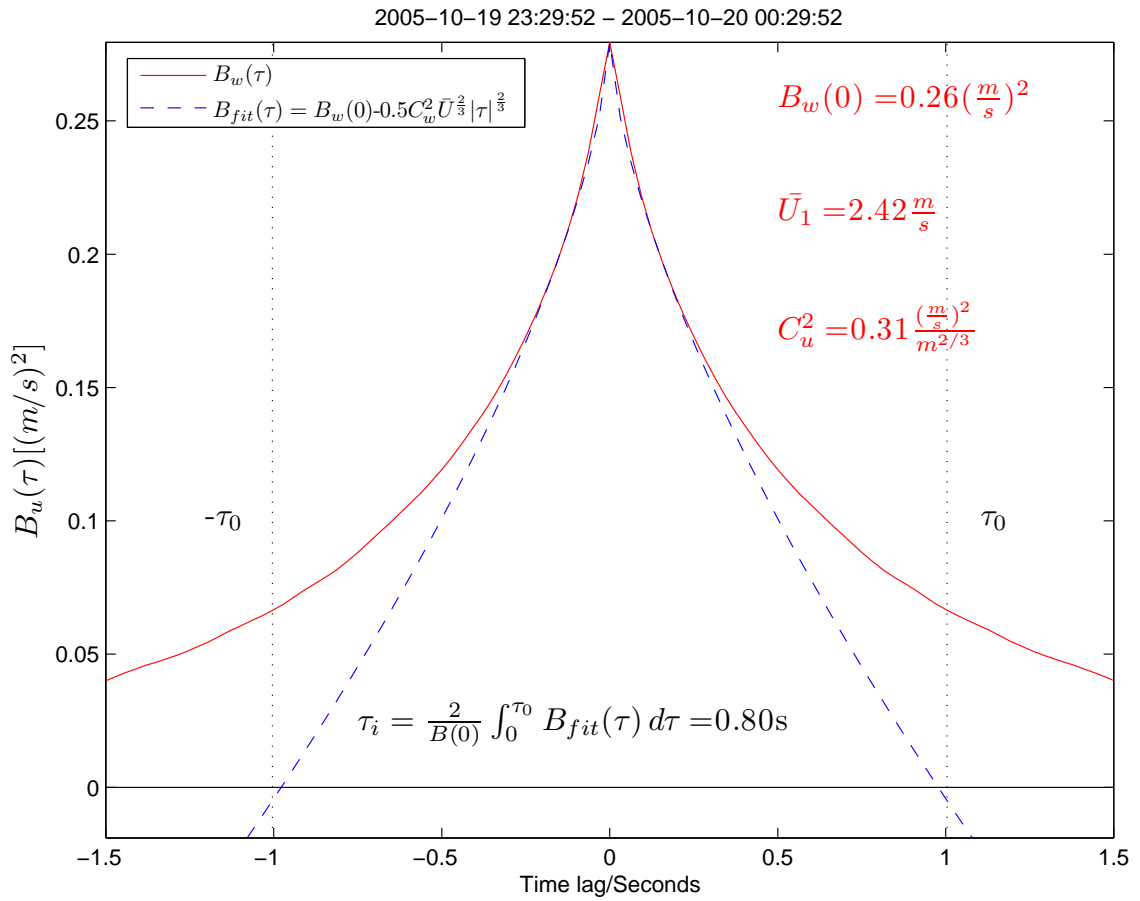


Figure 4.23. Autocovariance function $B_w(\tau)$ and integral time scale τ_{iw}

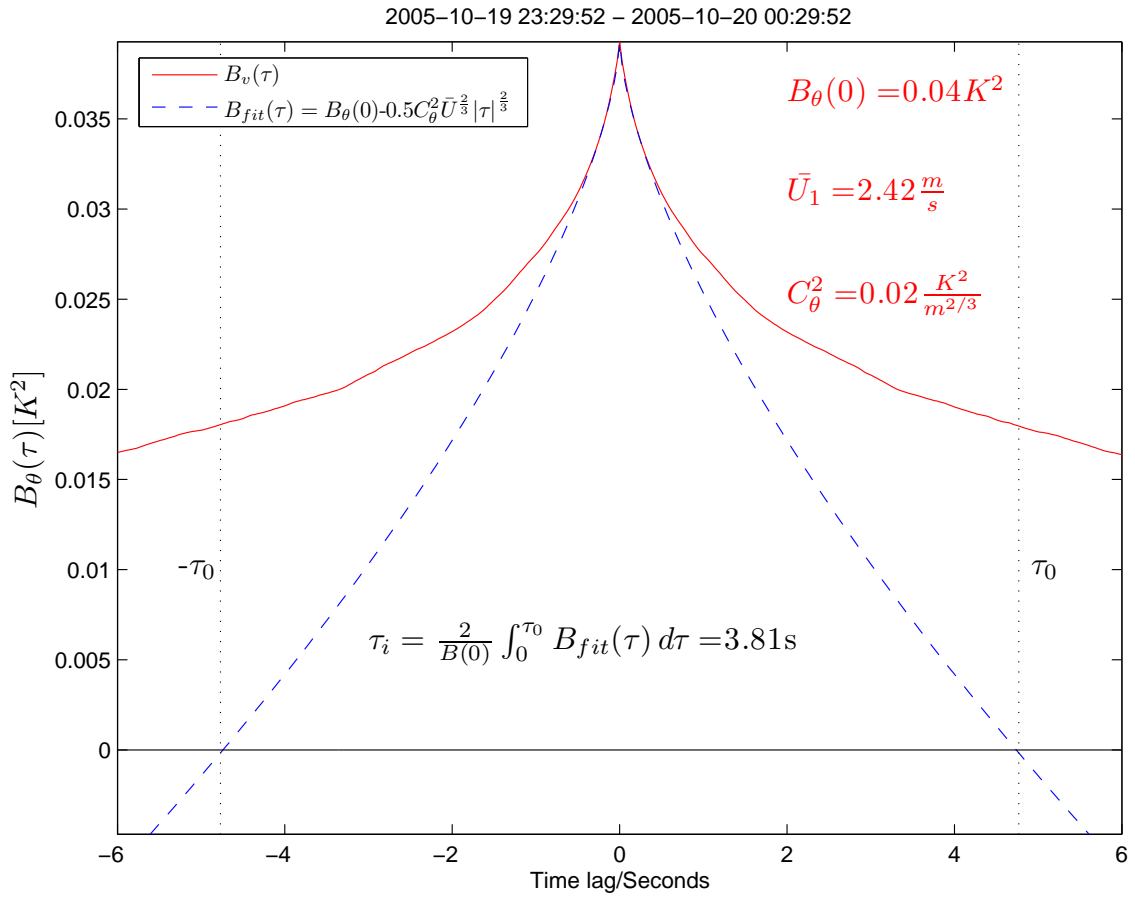


Figure 4.24. Autocovariance function $B_{\theta}(\tau)$ and integral time scale $\tau_{i\theta}$

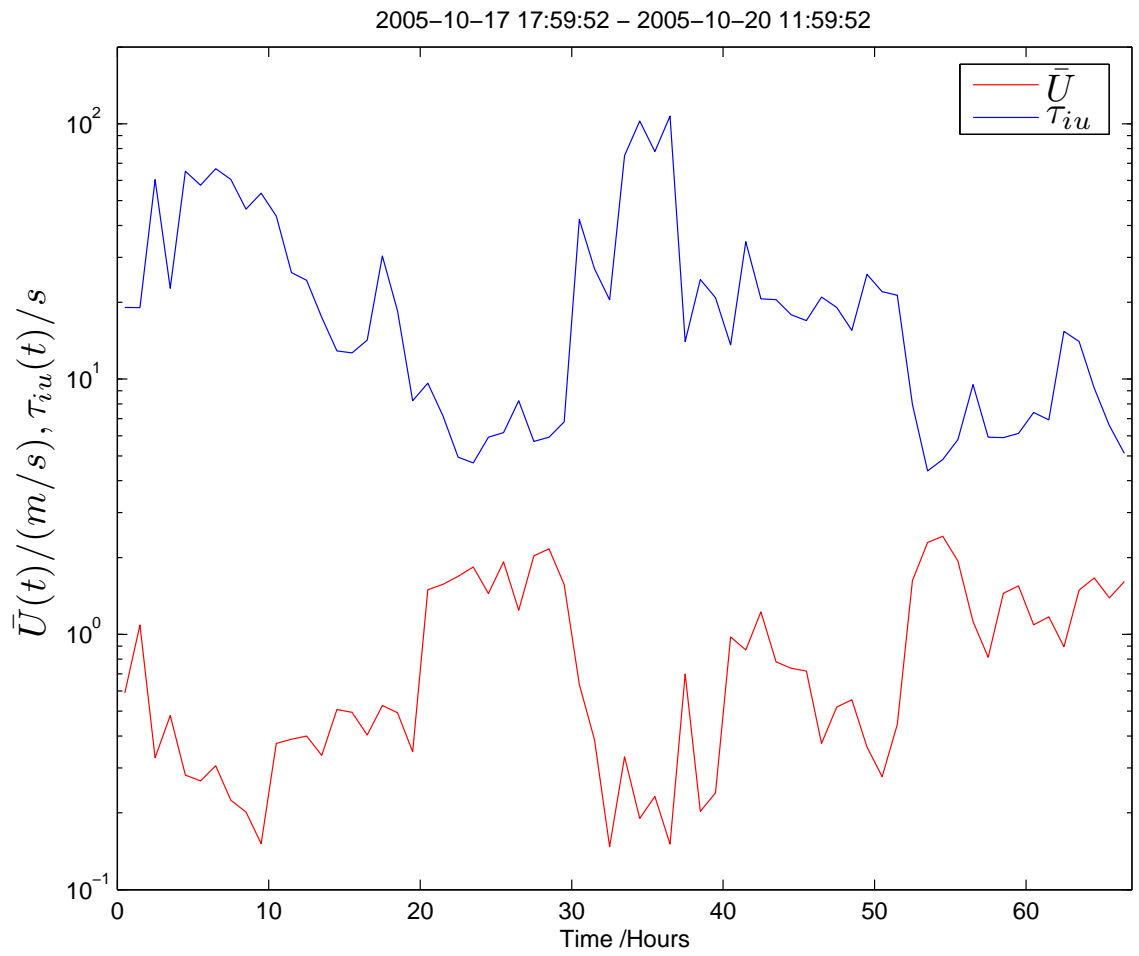


Figure 4.25. Integral time scale τ_{iu} and mean wind speed \bar{U}

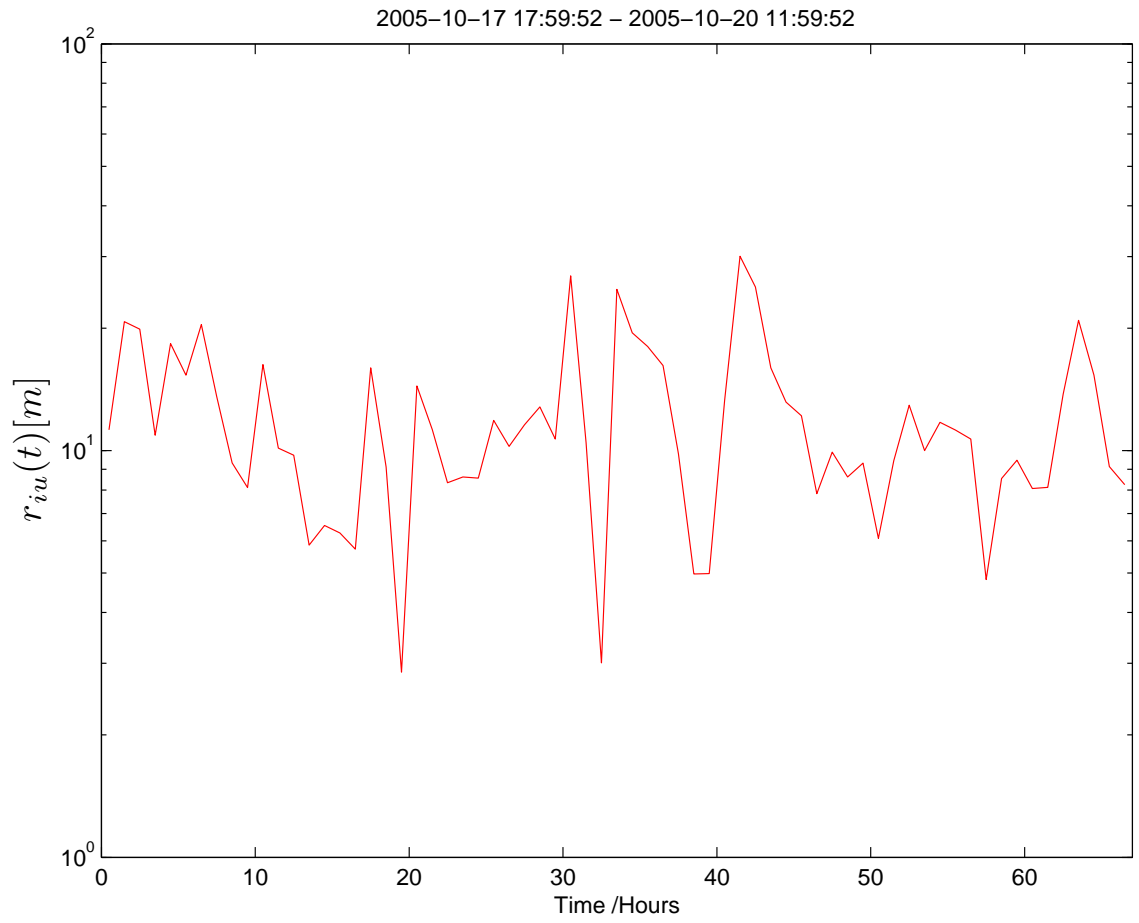


Figure 4.26. Integral length scale r_{iu}

4.5.7 Isotropy

Kolmogorov (1941a) predicts a 4/3 ratio between the longitudinal and the transverse correlation functions of the velocity in the inertial subrange for homogeneous and isotropic turbulence. Using equation [2.54] and Taylor's hypothesis, equation [2.39] can be written as:

$$\frac{D_w(\tau)}{D_u(\tau)} = \frac{D_v(\tau)}{D_u(\tau)} = \frac{4}{3}, \quad (4.60)$$

and

$$\frac{D_w(\tau)}{D_v(\tau)} = 1. \quad (4.61)$$

Therefore,

$$C_w^2 = C_v^2 = \frac{4}{3}C_u^2. \quad (4.62)$$

Inserting equation [4.49] and equation [4.50] accordingly:

$$\frac{D_w(\tau)}{D_v(\tau)} = \frac{S_w(\omega)}{S_v(\omega)} \quad (4.63)$$

and

$$\frac{D_w(\tau)}{D_u(\tau)} = \frac{D_v(\tau)}{D_u(\tau)} = \frac{S_w(\omega)}{S_u(\omega)} = \frac{S_v(\omega)}{S_u(\omega)}. \quad (4.64)$$

Figure 4.27 shows the ratios of the structure functions. In figure 4.28 the ratios of the power spectra are shown.

In figure 4.27 it can be seen that the 4/3 ratio is not exactly reached for the smallest time lag, which could be a result of spatial filtering (as a result of the finite size of the sonic) that attenuates the small scale turbulence. The sharper decline of $\frac{D_w(\tau)}{D_v(\tau)}$ compared to $\frac{D_v(\tau)}{D_u(\tau)}$ is a likely result of anisotropy of the w velocity component, due to the presence of the ground. The velocity components u and v , on the other hand, have more space available than the velocity component w , since they are oriented into the horizontal plane. Thus the isotropic behavior shown by $\frac{D_v(\tau)}{D_u(\tau)}$ is more extended than the one of $\frac{D_w(\tau)}{D_u(\tau)}$. A similar behavior can be seen in figure 4.28. The spike in figure 4.28 in the graph of $\frac{S_v(f)}{S_u(f)}$ at $f \approx 0.02$ Hz and

2005-10-19 23:29:52 – 2005-10-20 00:29:52

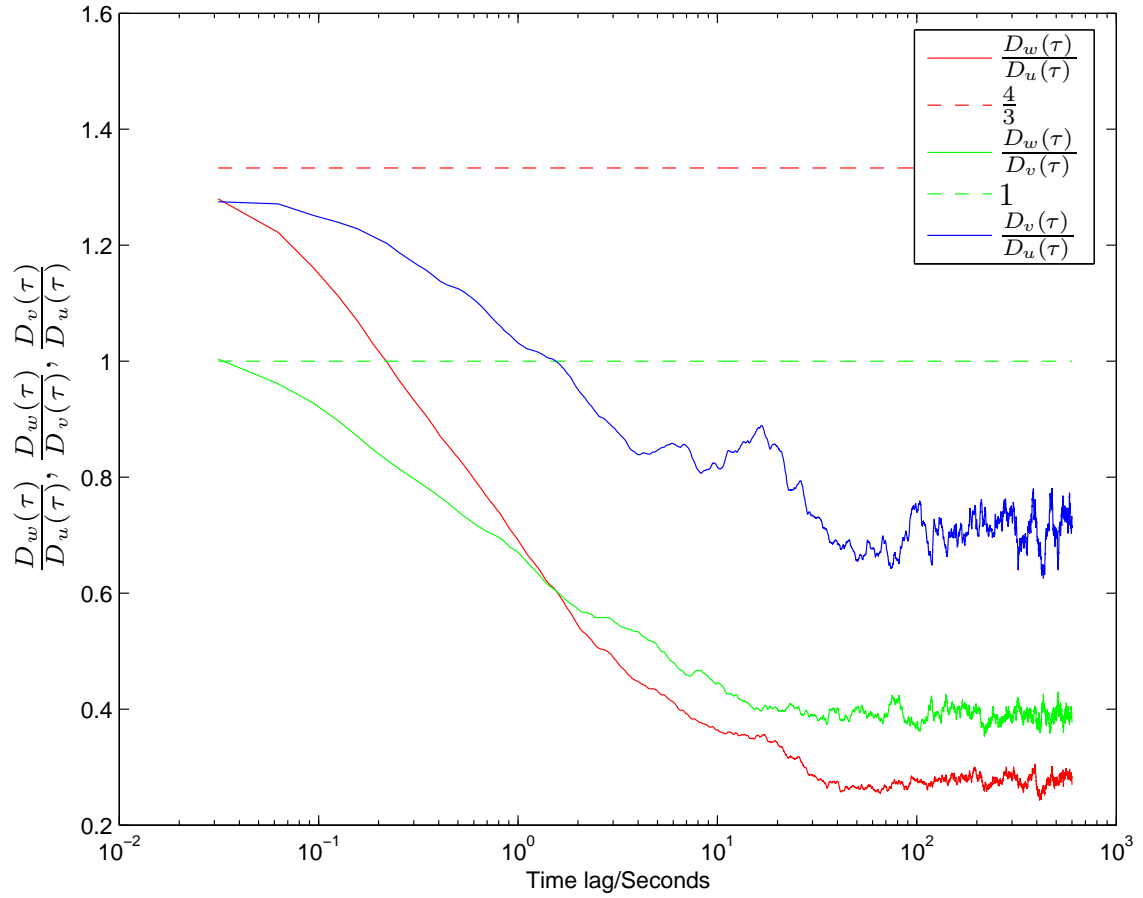


Figure 4.27. Ratios between structure functions

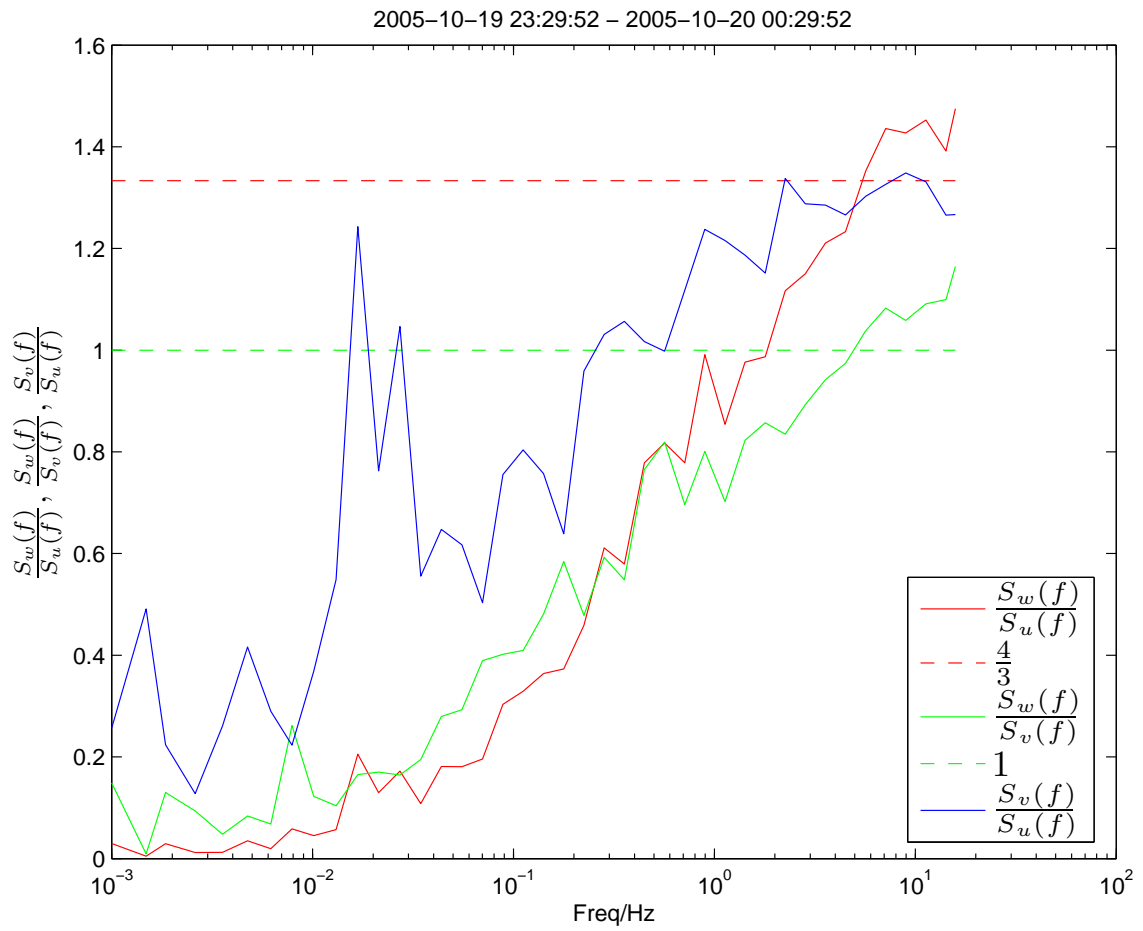


Figure 4.28. Ratios between power spectra

in figure 4.27 in graph $\frac{D_v(\tau)}{D_u(\tau)}$ at $\tau \approx 1.1$ s seems to be from a larger scale effect that is not directly related to small-scale turbulence.

CHAPTER 5

SUMMARY AND CONCLUSIONS

5.1 Summary

In chapter one, motivation for turbulence measurements in the surface layer was given and it was pointed out that the sonic anemometer is a good tool for such measurements. The historical development of turbulence research was outlined and the current state summarized. Chapter two reviewed the theory of locally homogeneous and isotropic turbulence and the Monin-Obukhov similarity theory. In chapter three the measurement system was described. In chapter four, 66 hours of wind velocity and temperature data including two diurnal cycles retrieved by means of two sonic anemometers and thermometers placed in the atmospheric surface layer at heights of 3 m and 3.8 m have been analyzed. The data was divided into 1 hour blocks. Following a rotation from the sonic coordinate system to a stream-wise coordinate system, a detrending algorithm was applied to the data, so that only the fluctuating parts were left. The periodograms of the wind velocity components, $\hat{S}_u(f)$, $\hat{S}_v(f)$, $\hat{S}_w(f)$, and the periodogram of the temperature, $\hat{S}_\theta(f)$, were resolved and presented by applying the FFT to the time series directly on the one hand and by computing the autocovariance function and using the Wiener-Khintchine relationship on the other hand. By means of logarithmic-equidistant-averaging of the periodograms the power spectra of the wind velocity components, $S_u(f)$, $S_v(f)$, $S_w(f)$, and the power spectrum of the temperature, $S_\theta(f)$, were estimated. The noise variances of the wind velocity components, σ_{un}^2 , σ_{vn}^2 , σ_{wn}^2 were estimated from the velocity spectra. The noise variance of the temper-

ature, $\sigma_{\theta n}^2$, was estimated from the power spectra *and* the autocovariance function. These noise variances were then used to compute the precision of the velocity and the temperature measurements. The temporal structure functions $D_u(\tau)$, $D_v(\tau)$, $D_w(\tau)$, $D_\theta(\tau)$ and spatial structure functions, $D_u(r)$, $D_v(r)$, $D_w(r)$, $D_\theta(r)$ of the velocity and temperature were computed. These and the power spectra were used (as two different ways) to estimate the structure parameters C_u^2 , C_v^2 , C_w^2 of the wind velocity components and the structure parameter C_θ^2 of the temperature. The integral time scales τ_{iu} , τ_{iv} , τ_{iw} of the wind velocity components and the integral time scale $\tau_{i\theta}$ of the temperature were computed from the autocovariance function. From the integral time scales, the integral length scales and the spectral widths were computed. The isotropic cut-off wavelength λ_c was estimated using the mean and the median of the integral length scale r_{iu} derived for all 66 hours of the data. Finally, the ratios of the structure functions, $\frac{D_w(\tau)}{D_u(\tau)}$, $\frac{D_w(\tau)}{D_v(\tau)}$, $\frac{D_v(\tau)}{D_u(\tau)}$ and the ratios of the frequency spectra $\frac{S_w(f)}{S_u(f)}$, $\frac{S_w(f)}{S_v(f)}$, $\frac{S_v(f)}{S_u(f)}$ were plotted against time lag and frequency, respectively.

5.2 Conclusions

We offer the following conclusions:

- (1) All power spectra follow a clear $-5/3$ law for nearly two decades, from about 0.2 Hz to the Nyquist frequency of about 16 Hz, which is consistent with Kolmogorov-type small scale turbulence. This finding is in agreement with earlier observations (e.g. Kaimal et al. (1972), Muschinski et al. (2004)). Below about 0.02 Hz the velocity spectra become flat. It can be seen that in this range the spectral power density of the vertical wind component w is about 10 times lower than the spectral power densities of the horizontal wind components u and v , which can be explained by the suppression of w fluctuations due to the presence of the ground.
- (2) It was found that our precisions (here defined as $\pm 3\sigma$ to include 99.7% of gaussian distributed errors) computed from the power spectra for the wind velocity components (u :

$\pm 0.249 \frac{\text{m}}{\text{s}}$, v : $\pm 0.279 \frac{\text{m}}{\text{s}}$, w : $\pm 0.303 \frac{\text{m}}{\text{s}}$) agree within an order of magnitude to the specification of the accuracy ($\approx \pm 0.1 \frac{\text{m}}{\text{s}}$) given by the manufacturer. However, our precision estimation is probably too conservative. For the precision of the temperature measurement it was found that the estimation based on the power spectrum and the autocovariance function agree very closely to each other. It was found to be about ± 0.078 K (about 25 times better than the specified accuracy of ± 2 K), which is comparable to (± 0.06 K) as found by Siebert and Muschinski (2001) for a similar, but different type of sonic.

(3) The integral length scales ($r_{iu} = 12.1$ m, $r_{iv} = 6.0$ m, $r_{iw} = 1.93$ m, $r_{i\theta} = 9.24$ m) and the integral time scales ($\tau_{iu} = 4.99$ s, $\tau_{iv} = 2.48$ s, $\tau_{iw} = 0.81$ s, $\tau_{i\theta} = 3.82$ s) were found to be consistent with the scale classification given by Orlanski (1975) for atmospheric turbulence, ($r_i \leq 20$ m and $\tau_i \leq 60$ s). It was found that the length scale r_{iu} is largest, as expected. Furthermore, it was found that the length scale r_{iw} is on the order of the height $z = 3$ m reduced by the roughness length z_0 .

(4) The isotropic cut-off wavelength was estimated as 12.05 m using the *mean* of the integral length scale of u and as 10.67 m using the *median* of the integral length scale of u . These are close to the theoretical estimate from Muschinski and Roth (1993) and Muschinski et al. (2004) given as $\lambda_c \approx 4z \approx 12$ m.

(5) The temperature and velocity structure parameters computed from the structure functions and the power spectra were found to agree with each other within about 35%. A typical expected range is given by Ishimaru (1978) on [p.344] as $C_\theta^2 = 10^{-6} \frac{K^2}{m^{2/3}}$ to $10^{-2} \frac{K^2}{m^{2/3}}$ for the temperature structure parameter and $C_u^2 = 10^{-4} \frac{(\frac{\text{m}}{\text{s}})^2}{m^{2/3}}$ to $1 \frac{(\frac{\text{m}}{\text{s}})^2}{m^{2/3}}$ for the velocity structure parameter. Similar orders of magnitudes for the structure parameters were obtained by Muschinski et al. (2004).

(6) A ratio close to 4/3 was observed for the ratio of the structure functions $\frac{D_v(\tau)}{D_u(\tau)}$ for time lags $\tau \leq 0.06$ s and for the ratio of the frequency spectra $\frac{S_v(f)}{S_u(f)}$ for frequencies $f \geq 2$ Hz. However, for the ratio of the structure functions $\frac{D_w(\tau)}{D_u(\tau)}$ and for the ratio of the frequency spectra $\frac{S_w(f)}{S_u(f)}$ the approach to the 4/3 ratio is present only at the smallest shown time lag

and for the highest shown frequency. The reason for this behavior, is the presence of the ground, which affects w more than u and v .

5.3 Recommendation and Future Work

For future work, the sonics should be used on more flat and homogeneous surface, to allow for more detailed statistical investigations. Some possible future experiments include the installations of several sonics placed at the same height, for the test of Taylor's hypotheses, by comparing the temporal and the spatial ACF or structure functions. Another experiment would place several sonics at significant different heights to further confirm the isotropic cut-off wavelength and to retrieve height profiles of velocity, temperature and the turbulent fluxes.

BIBLIOGRAPHY

- Foken, T., 2003: *Angewandte Meteorologie*. Springer, Berlin ; Heidelberg, 290 pp.
- Garratt, J. R., 1992: *The atmospheric boundary layer*. Cambridge University Press, Cambridge.
- Ishimaru, A., 1978: *Wave propagation and scattering in random media*. Academic Press, New York.
- Kaimal, J. C. and J. J. Finnigan, 1994: *Atmospheric boundary layer flows. Their structure and measurements*. Oxford University Press, Oxford, 289 pp.
- Kaimal, J. C., J. C. Wyngaard, Y. Izumi, and O. R. Cote, 1972: Spectral characteristics of surface-layer turbulence. *Quarterly Journal of the Royal Meteorological Society*, **98**, 563–589.
- Kolmogorov, A. N., 1941a: Dissipation of energy in the locally isotropic turbulence. *C. R. (Doklady) Acad. Sci. USSR*, **32**, 16–18.
- 1941b: The local structure of turbulence in incompressible viscous fluid for very large Reynolds number. *C. R. (Doklady) Acad. Sci. USSR*, **30**, 299–303.
- Monin, A. S., 1970: The atmospheric boundary layer. *Annual Review of Fluid Mechanics*, **2**, 225–250, doi:10.1146/annurev.fl.02.010170.001301.
- Monin, A. S. and A. M. Obukhov, 1954: Basic laws of turbulent mixing in the ground layer of the atmosphere. *Trans. Geophys. Inst. Akad. Nauk. USSR*, **54**, 163–187.
- Muschinski and Roth, 1993: A local interpretation of Heisenberg’s transfer theory. *Contr. Atmos. Phys.*, **66**, 335–346.
- Muschinski, A., R. Frehlich, M. Jensen, and et al., 2001: Fine-scale measurements of turbulence in the lower troposphere: An intercomparison between a kite- and balloon-borne, and a helicopter-borne measurement system. *Boundary-Layer Meteorology*, **98**, 219–250.
- Muschinski, A., R. G. Frehlich, and B. B. Balsley, 2004: Small-scale and large-scale intermittency in the nocturnal boundary layer and the residual layer. *Journal of Fluid Mechanics*, **515**, 319–351.

- Muschinski, A. and D. H. Lenschow, 2001: Meeting summary: Future directions for research on meter- and submeter-scale atmospheric turbulence. *Bulletin of the American Meteorological Society*, **82**, 2831–2844.
- Obukhov, A. M., 1941: Spectral energy distribution in a turbulent flow. *C. R. (Doklady) Acad. Sci. USSR*, **32**, 22–24.
- Orlanski, I., 1975: A rational subdivision of scales for atmospheric processes. *Bulletin of the American Meteorological Society*, **56**, 527–530.
- R.M. Young Company, 1999: *Model 81000 ultrasonic anemometer*. R.M. Young Company, 2801 Aero Park Drive, Traverse City, Michigan 49686, USA, rev b081303 edition.
- Siebert, H. and A. Muschinski, 2001: Relevance of a tuning-fork effect for temperature measurements with the Gill Solent HS ultrasonic anemometer-thermometer. *Journal of Atmospheric and Oceanic Technology*, **18**, 1367–1376.
- Simmons, L. F. G., C. Salter, and G. I. Taylor, 1938: An experimental determination of the spectrum of turbulence. *Royal Society of London Proceedings Series A*, **165**, 73–89.
- Tatarskii, V. I., 1961: *Wave propagation in a turbulent medium*. McGraw-Hill, New York.
- Tatarskii, V. I., 1971: *The effects of the turbulent atmosphere on wave propagation*. Jerusalem: Israel Program for Scientific Translations, 1971.
- Taylor, G. I., 1938: The spectrum of turbulence. *Royal Society of London Proceedings Series A*, **164**, 476–490.
- Wilczak, J. M., S. P. Oncley, and S. A. Stage, 2001: Sonic anemometer tilt correction algorithms. *Boundary-Layer Meteorology*, **99**, 127–150.
- Wyngaard, J. C., 1981: Cup, propeller, vane, and sonic anemometers in turbulence research. *Annual Review of Fluid Mechanics*, **13**, 399–423, doi:10.1146/annurev.fl.13.010181.002151.